AGU PUBLICATIONS

JGR

Journal of Geophysical Research: Space Physics

RESEARCH ARTICLE
10.1002/2014JA020239

Key Points:
- A Comprehensive Inner Magnetosphere-Ionosphere (CIMI) model has been developed
- CIMI solves for essential quantities in the inner magnetosphere and ionosphere
- Energization and loss for ring current radiation belts are identified by CIMI

Correspondence to:
M.-C. Fok,
mei-ching.h.fok@nasa.gov

Citation:
Fok, M.-C., N. Y. Buzulukova, S.-H. Chen, A. Glocer, T. Nagai, P. Valek, and J. D. Perez (2014), The Comprehensive Inner Magnetosphere-Ionosphere Model, *J. Geophys. Res. Space Physics*, *119*, 7522–7540, doi:10.1002/2014JA020239.

Received 3 JUN 2014
Accepted 1 SEP 2014
Accepted article online 3 SEP 2014
Published online 24 SEP 2014

The Comprehensive Inner Magnetosphere-Ionosphere Model

M.-C. Fok[1], N. Y. Buzulukova[1,2], S.-H. Chen[1,3], A. Glocer[1], T. Nagai[4], P. Valek[5], and J. D. Perez[6]

[1]NASA Goddard Space Flight Center, Greenbelt, Maryland, USA, [2]Center for Research and Exploration in Space Science and Technology, University of Maryland, College Park, Maryland, USA, [3]Center for Research and Exploration in Space Science and Technology, Universities Space Research Association, Columbia, Maryland, USA, [4]Department of Earth and Planetary Sciences, Tokyo Institute of Technology, Tokyo, Japan, [5]Southwest Research Institute, San Antonio, Texas, USA, [6]Physics Department, Auburn University, Auburn, Alabama, USA

Abstract Simulation studies of the Earth's radiation belts and ring current are very useful in understanding the acceleration, transport, and loss of energetic particles. Recently, the Comprehensive Ring Current Model (CRCM) and the Radiation Belt Environment (RBE) model were merged to form a Comprehensive Inner Magnetosphere-Ionosphere (CIMI) model. CIMI solves for many essential quantities in the inner magnetosphere, including ion and electron distributions in the ring current and radiation belts, plasmaspheric density, Region 2 currents, convection potential, and precipitation in the ionosphere. It incorporates whistler mode chorus and hiss wave diffusion of energetic electrons in energy, pitch angle, and cross terms. CIMI thus represents a comprehensive model that considers the effects of the ring current and plasmasphere on the radiation belts. We have performed a CIMI simulation for the storm on 5–9 April 2010 and then compared our results with data from the Two Wide-angle Imaging Neutral-atom Spectrometers and Akebono satellites. We identify the dominant energization and loss processes for the ring current and radiation belts. We find that the interactions with the whistler mode chorus waves are the main cause of the flux increase of MeV electrons during the recovery phase of this particular storm. When a self-consistent electric field from the CRCM is used, the enhancement of MeV electrons is higher than when an empirical convection model is applied. We also demonstrate how CIMI can be a powerful tool for analyzing and interpreting data from the new Van Allen Probes mission.

1. Introduction

Since the discovery of the radiation belts [*Van Allen*, 1959], this energetic particle population has been a subject of intense study. Many space-borne missions carried instruments to measure the energetic electron and ion fluxes through the radiation belt ring current region, e.g., Akebono, Solar, Anomalous, and Magnetospheric Particle Explorer, Los Alamos National Laboratory, GOES, CRRES, Polar, Time History of Events and Macroscale Interactions during Substorms (THEMIS) [*Takagi et al*., 1993; *Baker et al*., 1985, 1993; *Higbie et al*., 1978; *Johnson and Ball*, 1992; *Acuna et al*., 1995; *Angelopoulos*, 2008; *Sibeck and Angelopoulos*, 2008], and the recent Van Allen Probes mission [*Mauk et al*., 2012]. It is of great scientific and practical interests to understand and be able to predict the variations and dynamics of the radiation belts and ring current.

Many studies have found a close relationship between solar interplanetary structures and particle fluxes in the radiation belts and ring current. *Reeves et al*. [2003] found that approximately half of all moderate and intense storms caused a net increase in the flux of energetic electrons by a factor of 2 or more; approximately a quarter of these storms resulted in a net decrease in the fluxes by more than a factor of 2. They also found that a higher solar wind velocity increased the probability of a large flux increase. *Denton and Borovsky* [2012] examined magnetospheric responses to strong ($v \sim 600$ km/s, duration ~ 4–5 days) and weak ($v \sim 500$ km/s, duration ~ 2 days) high-speed solar wind streams (HSSs). They found the average MeV electron flux at the end of weak HSS events to be lower than the flux level measured before the arrival of the HSS. In contrast, the MeV electron flux increased after a strong HSS.

The radiation belts and ring current behave differently during coronal mass ejection (CME) driven and corotating interaction region (CIR) driven storms. *Borovsky and Denton* [2006] tabulated differences between CME and CIR storms. They found strong ring current (*Dst*) in CME storms but higher relativistic electron flux during CIR storms. By examining relativistic electron fluxes during 46 CME- and 6 CIR-associated storms,

Kataoka and Miyoshi [2006] also found that, on average, CIR storms were more effective in relativistic electron enhancement. CME-driven storms usually result in a stronger ring current as indicated by the *Dst* index. *Turner et al*. [2009], however, found that CIR storms were more geo-efficient in the sense that the ratio of the energy deposited in the magnetosphere and ionosphere to the energy input from the solar wind is higher than for CME storms.

The statistical studies mentioned above give us a general and an averaged picture of how the radiation belts and the ring current respond to a variety of solar wind conditions. The response of these energetic particles to an individual storm, however, is still far from predictable. The main problem is the lack of physical understanding. It is not clear why high solar wind velocity and fluctuations are favorable conditions for radiation belt flux enhancement. It may be caused by the associated strong ULF waves and thus strong radial diffusion; or the enhancement could be a result of an elevated plasma sheet temperature driven by the high-speed streams. It is also not understood what physical mechanisms are responsible for the decreased MeV electron flux relative to prestorm level in some weak HSS events. There are still other questions about why relativistic electrons behave differently during CME and CIR storms. Furthermore, we need to understand the role of magnetosphere-ionosphere (M-I) coupling in regulating the flux enhancements during storms. To gain physical insights to such unresolved scientific questions, model simulations along with extensive data-model comparison have proven to be a very promising approach [i.e., *Buzulukova et al*., 2008; *Ebihara et al*., 2008; *Fok et al*., 2003; *Glocer et al*., 2011; *Jordanova et al*., 2010; *Garner et al*., 2004].

A number of models have been established to simulate the radiation belt and ring current dynamics and to provide an interpretation of the observable features. Kinetic formulation is a commonly used technique. In a kinetic model, the equation describing particle distribution functions is solved analytically or numerically. For example, the Comprehensive Ring Current Model (CRCM) was established to solve the ring current particle distributions and consider the closure of electric current between the magnetosphere and the ionosphere [*Fok et al*., 2001b]. The CRCM has been used to simulate a number of idealized and real events [*Fok et al*., 2001b, 2003; *Ebihara and Fok*, 2004; *Ebihara et al*., 2005; *Buzulukova et al*., 2008, 2010]. Many noticeable signatures are reproduced such as ion flux postmidnight enhancement, subauroral polarization stream, and ring current shielding/over-shielding [*Fok et al*., 2001b, 2003; *Ebihara and Fok*, 2004; *Buzulukova et al*., 2010]. A plasmasphere model is embedded in the CRCM and the convection of the cold plasmas is driven by the electric field calculated from the CRCM [*Fok et al*., 2005]. With the consideration of ionosphere feedback, the CRCM successfully simulated the global structures of the plasmasphere, such as drainage plumes and the propagation of undulations from the nightside to dayside local times [*Fok et al*., 2005; *Buzulukova et al*., 2008].

The Radiation Belt Environment (RBE) model, on the other hand, was developed to calculate radiation belt particle fluxes and to predict their variations during active times [*Fok et al*., 2001a, 2005, 2008, 2011a; *Zheng et al*., 2003; *Glocer et al*., 2009]. The RBE model calculates the distribution functions of 10 keV to 4 MeV electrons and considers diffusive interactions with whistler mode chorus waves. The model was also used to simulate a substorm injection during a dipolarization of the magnetic field [*Fok et al*., 2001a]. Observable features during substorms, such as dispersionless injection and drift echoes, were successfully reproduced. The electron flux enhancements during magnetic storms were also studied using the RBE model [*Zheng et al*., 2003; *Fok et al*., 2005, 2008]. It was found that the energization by the inductive electric field and by whistler mode chorus waves is both crucial for the flux increase during magnetic storms. Pitch angle diffusion by chorus waves was also found to be the major loss mechanism for ring current electrons [*Fok et al*., 2011a].

Both the CRCM and RBE are well-established models. Many scientific insights have been obtained by simulations using these two models; however, they still have their own limitations. Early RBE studies were performed using empirical electric field models [*Zheng et al*., 2003; *Fok et al*., 2008]. In the CRCM, the loss rate of electrons is simply assumed to be a fraction of strong diffusion rate [*Buzulukova et al*., 2010; *Gkioulidou et al*., 2012]. It is a natural progression to merge the CRCM and RBE to combine the merits of both models. With such a model, the distribution function of ring current electrons (seed population for radiation belt electrons) is simulated in a self-consistent electric field model with a precise treatment of wave-particle interactions. The accurate models of convection and wave diffusion for ring current electrons result in a realistic specification of electron precipitation in the ionosphere, which in turn, modifies the ionospheric conductance and convection pattern. The coupled model thus represents a Comprehensive Inner Magnetosphere-Ionosphere model (named as CIMI) that calculates distribution functions of ring current ions,

ring current and radiation belt electrons, plasmaspheric density, subauroral convection field, Region 2 field-aligned current, and electron precipitation in the ionosphere.

In this paper, we will describe the formulation of CIMI based on the CRCM and RBE models. We have performed a CIMI simulation for the storm on 5–9 April 2010 and then compared our results with data from the Two Wide-angle Imaging Neutral-atom Spectrometers (TWINS) and Akebono satellites. We show the advantages of this coupled model in reproducing the observable features. We also demonstrate how CIMI can be a powerful tool for analyzing and interpreting data from the Van Allen Probes mission.

2. The Comprehensive Inner Magnetosphere-Ionosphere Model

The CIMI model combines the CRCM [*Fok et al*., 2001b] and the RBE model [*Fok et al*., 2011a] to obtain energetic ion (0.1 keV–400 keV) and electron (1 keV–4 MeV) distributions, Region 2 field-aligned currents, subauroral ionospheric potentials, and plasmaspheric densities. The CIMI model solves the same kinetic equation of particle species as that in the RBE model, except with the inclusion of a charge-exchange loss term for ions. On the other hand, CIMI employs the CRCM algorithm in solving the ionospheric potential. The three major equations solved in CIMI are (1) the bounce-averaged Boltzmann equation for distribution functions of ring current and radiation belt particles, *fs*; (2) the ionospheric current conservation equation for the ionospheric potential, Φ; and (3) the equation for the total plasmasphere ion content per unit magnetic flux, *N*:

$$\frac{\partial f_s}{\partial t}+\langle\dot{\lambda}_i\rangle\frac{\partial f_s}{\partial \lambda_i}+\langle\dot{\phi}_i\rangle\frac{\partial f_s}{\partial \phi_i}=\frac{1}{G}\frac{\partial}{\partial \alpha_o}\left[G\left(D_{\alpha_o\alpha_o}\frac{\partial f_s}{\partial \alpha_o}+D_{\alpha_o E}\frac{\partial f_s}{\partial E}\right)\right]+\frac{1}{G}\frac{\partial}{\partial E}\left[G\left(D_{EE}\frac{\partial f_s}{\partial E}+D_{E\alpha_o}\frac{\partial f_s}{\partial \alpha_o}\right)\right]-\nu\sigma_{sH}\langle n_H\rangle f_s-\left(\frac{f_s}{0.5\tau_b}\right)_{\substack{\text{loss}\\ \text{cone}}} \tag{1}$$

$$\nabla\cdot\left(-\overleftrightarrow{\Sigma}\nabla\Phi\right)=J_{||}sinI \tag{2}$$

$$\frac{\partial N}{\partial t}+\langle\dot{\lambda}_i\rangle\frac{\partial N}{\partial \lambda_i}+\langle\dot{\phi}_i\rangle\frac{\partial N}{\partial \phi_i}=\frac{F_n+F_s}{B_i} \tag{3}$$

where

$$G=T(\alpha_o)\sin 2\alpha_o(E+E_o)\sqrt{E(E+2E_o)}$$

Equation (1) solves for the average distribution function, $f_s=f_s(t,\lambda_i,\phi_i,M,K)$, between the mirror points on a specified field line. The magnetic latitude at the base of the magnetic field line is given by λ_i and the local time at the base of the field line is given by ϕ_i. *M* is defined to be the relativistic magnetic moment, and $K=J/\sqrt{8m_oM}$ where *J* is the second adiabatic invariant. Field lines are labeled, using a subscript *i*, by their ionospheric foot points. The drift across field lines describes how the particles move. The inner boundary of the model is set at 12° magnetic latitude, which corresponds to $L=1.06$. The outer boundary is defined by field lines with latitude no greater than 70.3° and an equatorial crossing at 10 Earth radii (R_E), whichever is closer. E_o is the rest energy, α_o represents equatorial pitch angle, and $T(\alpha_o)$ is a function depending on α_o and the shape of the field line.

The drifts of particle populations are represented by the leftside of equation (1) while the diffusion and loss processes appear on the rightside. *Fok and Moore* [1997] describe in detail the calculation of the bounce-averaged drift velocities across field lines, $\langle\dot{\lambda}_i\rangle$ and $\langle\dot{\phi}_i\rangle$. These drifts include the gradient-curvature drift, $E\times B$ drift from convection, and corotation electric fields. The effects of the inductive electric field resulting from a time-varying magnetic field are accounted for implicitly as described by *Fok et al*. [2005].

Particle diffusion in energy and pitch angle due to interactions with plasma waves are accounted for by the first and second terms on the right of equation (1). We first map the particle phase space density from the (*M*, *K*) to (E, α_o) coordinates when solving these terms. The diffusion is performed in E and α_o coordinates and then the updated distribution is mapped back to the (*M*, *K*) coordinates [*Fok et al*., 1996, 2011a]. The last two terms on the right-hand side of equation (1) represent charge exchange loss (for ions only) and the losses due to precipitation in the loss cone. The boundary for the loss cone corresponds to a mirror location of

100 km altitude. The charge-exchange cross section for a species s with neutral hydrogen is labeled by σ_{sH}. The term $\langle n_H \rangle$ is the density of hydrogen averaged over a bounce and τ_b is the particle bounce period. We assume that in the loss cone, particles have a lifetime of 0.5 τ_b [*Lyons*, 1973].

Equation (1) is an initial boundary problem. For ions, we use zero initial distribution or initial fluxes specified based on the empirical model of quiet time ring current by *Sheldon and Hamilton* [1993]. The initial distribution for electrons is given by the empirical model of AE8 [*Vette*, 1991; *Fung*, 1996]. Isotropic pitch angle distribution is assumed at the beginning of simulation. Particle flux at the inner boundary at $L = 1.06$ is set to be zero. Distribution at the outer boundary is specified by empirical plasma sheet models [*Ebihara and Ejiri*, 2000; *Borovsky et al*., 1998; *Tsyganenko and Mukai*, 2003] or provided by global magnetohydrodynamics (MHD) models [*Glocer et al*., 2013a; *Meng et al*., 2013]. When solving the diffusion terms in equation (1), we assume $\partial f/\partial E = 0$ at energy lower limit and $f = 0$ at the upper limit, and $\partial f/\partial \alpha_o = 0$ is applied to both ends of the pitch angle grid.

The 2-D thin-shell approximation, allows us to use equation (2) to express ionospheric current conservation [*Toffoletto et al*., 2003]. $\overleftrightarrow{\Sigma}$ is a tensor representing ionospheric Hall and Pedersen conductance. is the ionospheric potential, I is the magnetic dip angle, and $J_{||}$ is the Region 2 current, which is calculated from the pressure gradients of all ring current species [*Fok et al*., 2001b]. CIMI thus solves the convection field self-consistently with the consideration of electric coupling between the magnetosphere and ionosphere. We specify the potential at the poleward boundary at 70.3° latitude by the Weimer 2K model [*Weimer*, 2001] and assume no current flowing across the equatorward boundary.

The CIMI model has an embedded plasmasphere model as described in equation (3). *Fn* and *Fs* are the ionospheric fluxes in or out of the flux tube at northern and southern ionospheres, and *Bi* is the magnetic field at the ionospheric foot points of the flux tube. The net flux of plasma in and out of a flux tube depends on the dayside refilling rate and the diffusion lifetime on the nightside [*Fok et al*., 2005]. As shown in the left-hand sides of equations (1) and (3), the plasmasphere particles drift in the same way as the energetic particles, except magnetic drift of cold plasma is ignored. We impose a saturation density at the model inner boundary and a plasma trough density at the outer boundary [*Carpenter and Anderson*, 1992]. We have assumed that plasma density is constant along a field line. The simulated plasmasphere density is used to calculate the wave diffusion coefficients [*Fok et al*., 2008, 2011a].

Figure 1 shows the major output from the CIMI model. Figures 1a and 1b are examples of equatorial electron, H^+, and O^+ fluxes. Figures 1c and 1d are the corresponding pitch angle distributions (PAD), from which 3-D fluxes can be constructed along field lines. The two top-right panels are electron precipitating energy flux and mean energy at the ionosphere. They are calculated by electron loss at the loss cone (last term of equation (1); ion precipitation is not shown). Figures 1i and 1j portray the CIMI calculated Region 2 currents (colors), convection potential (contours) at the ionosphere, and potential mapped to the equator under the assumption of zero electric field along a field line. A typical map of the plasmasphere density is shown in Figure 1k. A sharp plasmapause in the premidnight sector and a plume structure extending from dusk to the dayside are clearly seen in the plot.

Since the CIMI and RBE models solve the same kinetic equation (equation (1)), the code verification for the RBE model should also be applied to the CIMI model. A detailed verification of energy and particle conservation of the RBE code was presented in *Liemohn et al*. [2012]. They found that the RBE code is able to handle localized injection. We are confident that, alike the RBE code, the CIMI model is numerically accurate and capable to resolve fine structures in the ring current and outer radiation belt.

3. The Storm on 5–9 April 2010

The geomagnetic storm on 5–9 April 2010 was triggered by the arrival of a fast CME [*Möstl et al*., 2010]. Figure 2 displays the solar wind *By*, *Bz*, speed, and density from the ACE satellite and geomagnetic indices on 5–9 April 2010. The solar wind parameters in Figure 2 have been shifted to the subsolar point. A substorm growth phase was observed on 5 April at ~0845 UT, shortly after the CME-associated shock hit and compressed the magnetosphere [*Connors et al*., 2011]. At this time, the interplanetary magnetic field (IMF) was very strong and fluctuated in direction. From 12:05 UT on 5 April, the magnetic cloud inside the CME interacted with the magnetosphere and produced a moderate storm with minimum *Dst* reaching −81 nT at 15:00 UT on 6 April.

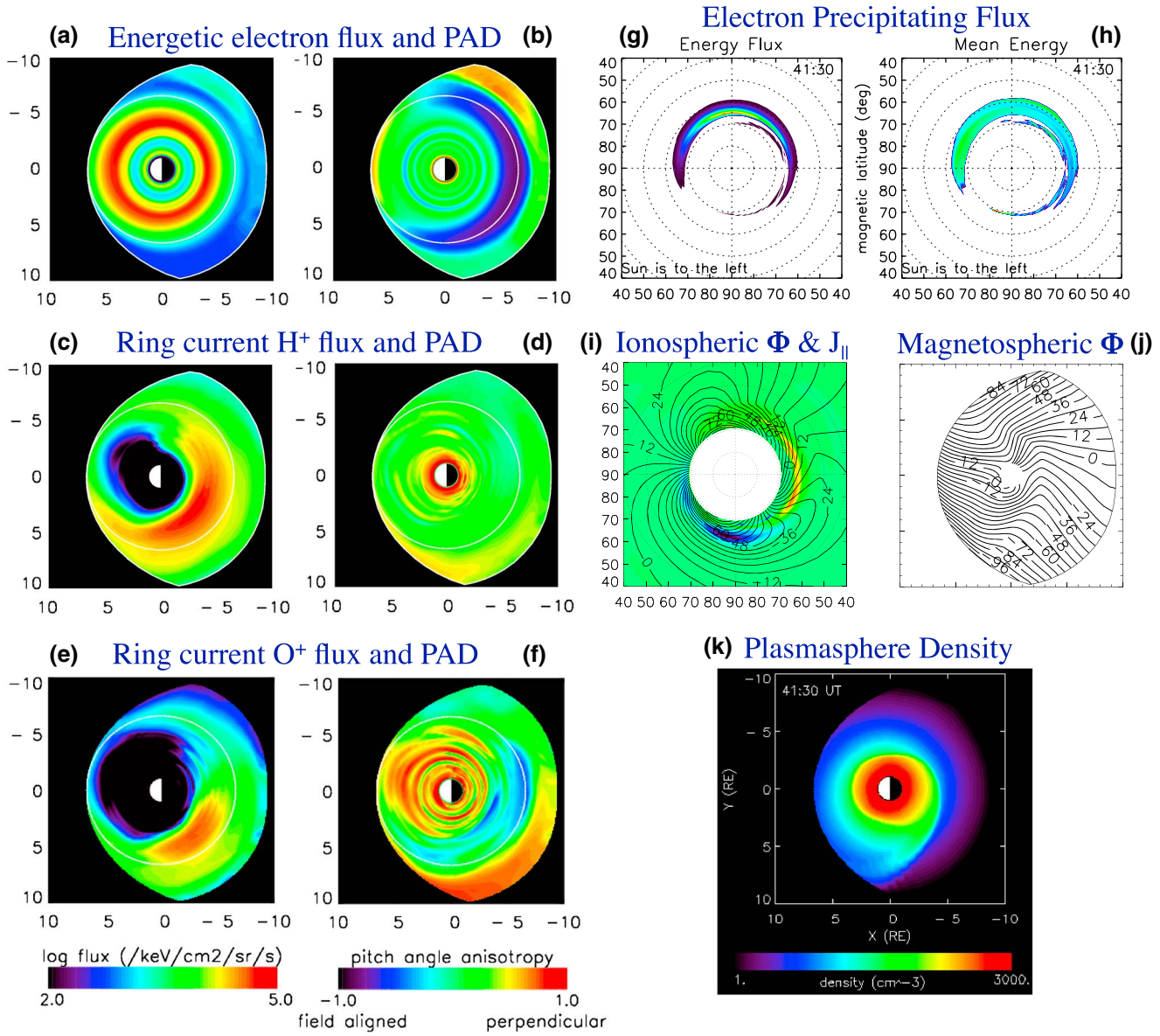

Figure 1. Major output from the CIMI model: (a) equatorial electron, (c) H^+, and (e) O^+ fluxes and (b, d, and f) the corresponding pitch angle distributions, (g) electron precipitating energy flux and (h) mean energy at the ionosphere, (i) Region 2 currents (colors) and convection potential (contours) at the ionosphere, (j) convection potential at the equator, and (k) the plasmasphere density at the equator. The Sun is on the left for all panels.

The development of energetic particles during the strong substorm which happened on 5 April 2010 was monitored by the Interstellar Boundary Explorer (IBEX) and the Two Wide-angle Imaging Neutral-atom Spectrometers (TWINS). Both satellites are equipped with energetic neutral atom (ENA) imagers. IBEX detected sharply enhanced ENA emissions as the dayside magnetosphere was compressed by the interplanetary shock at ~0826 UT. About 15 min later, TWINS observed strong ring current and low-altitude ENA emissions [*McComas et al.*, 2012]. This was the first study to combine IBEX and TWINS observations to provide a global picture of the magnetospheric response to an interplanetary shock. Stereo images from TWINS 1 and 2 on 6 April 2010 were analyzed by *Goldstein et al.* [2012]. They found local time dependence of ring current pitch angle anisotropy with strong anisotropy on the duskside. In another study, *Goldstein et al.* [2013] examined the energy spectra of low-altitude emissions on 6 April from the two TWINS satellites. They reported spectra shifting to higher energies for emissions from more westward magnetic local time (MLT).

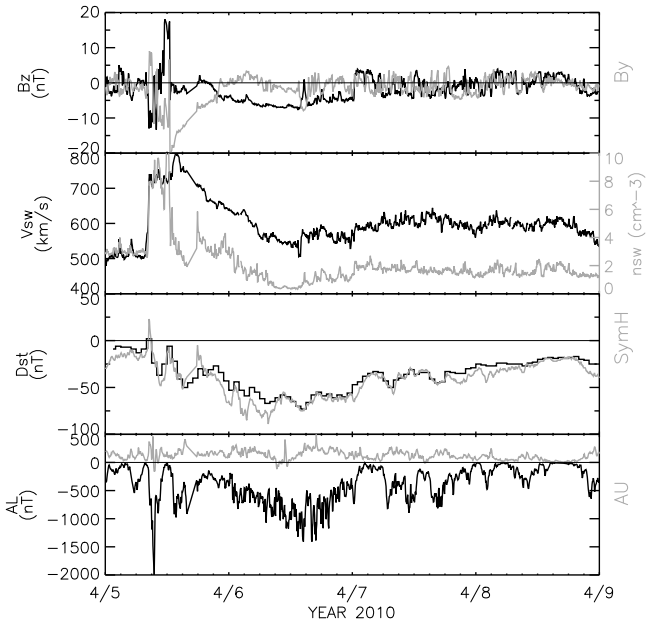

Figure 2. IMF *Bz*, *By*, solar wind speed, and density measured from the ACE satellite, and *Dst*, *SYM-H*, *AL* and *AU* on 4–9 April 2010. The ACE data are 44 min shifted in time.

3.1. CIMI Simulation of the Storm on 5–9 April 2010

We have simulated the 5–9 April 2010 storm with the CIMI model. The Tsyganenko 2004 (T04) model [*Tsyganenko et al*., 2003; *Tsyganenko and Sitnov*, 2005] was used to specify the magnetic field configuration. The temporal variations of the magnetic field were controlled by the time-varying model input parameters: *Dst*, solar wind ram pressure, *By*, and *Bz*. We updated the magnetic field every 5 min. The Weimer 2K model [*Weimer*, 2001] was used to determine the potential at CIMI's polar boundary at the ionosphere at 70.3° magnetic latitude (MLAT). The model of *Hardy et al*. [1987] was used to specify the auroral conductance. The ion distribution at the equatorial outer boundary was assumed to be a Maxwellian with density (N_{ps}) and temperature (T_{ps}) given by linear relations with the upstream solar wind condition [*Ebihara and Ejiri*, 2000; *Borovsky et al*., 1998]:

$$\begin{aligned} N_{ps}(t) &= 0.395 + 0.025N_{sw}(t-2h) \\ T_{ps}(t) &= -3.65 + 0.019V_{sw}(t-2h) \end{aligned} \tag{4}$$

where N_{ps} is in cm^{-3}, N_{sw} is the solar wind density in the same unit, T_{ps} is in keV and V_{sw} is the solar wind speed in km/s. We assumed a 2 h response time for changes in the boundary condition to solar wind variations. The electron distribution at the outer boundary was assumed to be a kappa function with $\kappa = 3$. Electron density was set to be the same as that of the ions, and the electron characteristic energy was lower than the ion temperature by a factor of 7.8 [*Baumjohann et al*., 1989]. In the calculation of charge exchange loss for ions, the spherical symmetric model of *Rairden et al.* [1986] is used to estimate the bounce-averaged neutral hydrogen density ($\langle n_H \rangle$ in equation (1)).

We considered electron diffusion due to interactions with lower band chorus waves and plasmaspheric hiss (first two terms on the right-hand side of equation (1)). The presence of chorus waves was assumed to be confined between −15° and 15° magnetic latitude. The pitch angle and energy diffusion coefficients were evaluated according to bounce- and drift-average quasi-linear theory [*Albert et al*., 2009]. The frequency and wave normal angle distributions were represented by truncated Gaussians. The peak, width, lower cutoff, and upper cutoff for ω and $x = \tan\theta$ were $(\omega_m, \delta\omega, \omega_{LC}, \omega_{UC}) = (0.35, 0.15, 0.125, 0.575)$ f_{ce} and $(x_m, \delta x, x_{\min}, x_{\max}) = (0, \tan 30°, 0, 1)$, where f_{ce} is the electron cyclotron frequency at the equator. The diffusion coefficients were calculated as a function of electron energy, equatorial pitch angle, *L* shell, and f_{pe}/f_{ce}, where f_{pe} is the electron plasma frequency. The diffusion coefficients were then scaled with a wave amplitude of 100 pT. To obtain the actual coefficients, we estimated the chorus intensity at a given location and time during the storm using the survey of plasma wave data from multiple satellite observations presented by *Meredith et al.* [2012]. The wave data were binned in *L* shell, magnetic local time, latitude (equatorial: within 15° off the equator, and midlatitude: 15°–30° off the equator), and by three levels of substorm activity ($AE < 100$ nT; $100 \le AE < 300$ nT; $AE \ge 300$ nT).

Similar to the coefficients for chorus waves, the hiss coefficients were calculated as a function of electron energy, equatorial pitch angle, *L* shell, and f_{pe}/f_{ce} [*Albert,* 2005, 2008; *Albert et al*., 2009]. The

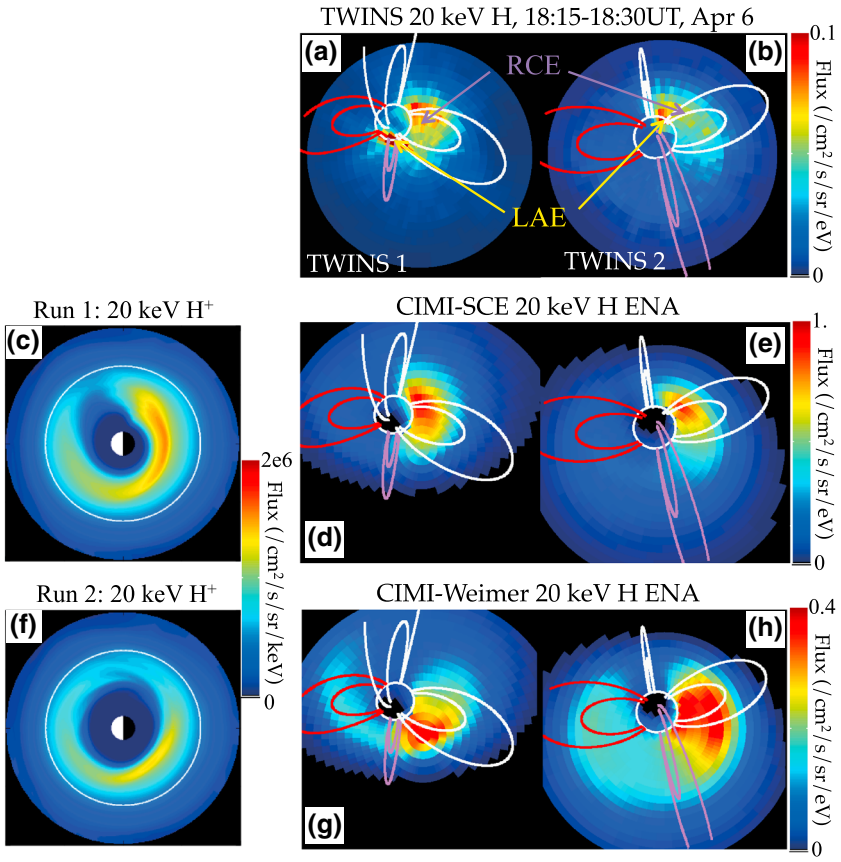

Figure 3. Comparison of TWINS ENA fluxes with CIMI simulated fluxes: (a and b) 20 keV H fluxes from TWINS 1 and 2 at 18:15–18:30 UT on 6 April 2010; (c–e) simulated equatorial flux of 20 keV H^+ from Run 1 with self-consistent electric (SCE) field and the corresponding ENA fluxes seen by TWINS 1 and 2; and (f–h) simulated ion and ENA fluxes from Run 2 with Weimer field.

peak, width, lower cutoff, and upper cutoff for ω and $x = \tan\theta$ were $(\omega_m, \delta\omega, \omega_{LC}, \omega_{UC}) = (550, 300, 100, 2000)$ Hz and $(x_m, \delta x, x_{\min}, x_{\max}) = (0, 0.36, 0, 0.58)$, respectively. The coefficients were normalized with an amplitude of 10 pT. To get the actual values of diffusion coefficients, we used the survey based on the CRRES observations for hiss waves [*Meredith et al.*, 2004]. The data were binned in *L*, *MLT*, and *AE*. We apply chorus wave diffusion outside the plasmasphere and hiss diffusion inside the plasmapause, which is defined by plasmasphere density of 20 cm^{-3}. We start the wave diffusion and plasmasphere density calculations at $t = 5$ h when the system reaches a roughly equilibrium stage.

There is good data coverage on the TWINS and Akebono spacecraft during the 5–9 April 2010 storm. We compare our simulation results with data from these satellites. The comparisons serve as validation of the CIMI model. Furthermore, by analyzing the simulation results, we gain insight into what mechanisms are responsible for the buildup and decay of the ring current and radiation belts during a magnetic storm.

3.2. CIMI Results Compared With TWINS Data

TWINS 1 and 2 are orbiting the Earth in Molniya orbits. Their high inclination and long residence time near the apogee put them in excellent positions to image the ring current. During the main and early recovery phase of the storm on 6 April 2010, the development of the ring current was continuously monitored by either TWINS 1 or 2. In some periods of time, both TWINS 1 and 2 were at favorable vantage points that stereo images of the ring current were captured. Figures 3a and 3b show the fish-eye views of 20 keV ENA images taken by TWINS 1 and 2 at 18:15–18:30 UT on 6 April. In each image, the white circle is the Earth rim. Dipole field lines of $L = 4$ and 8, at four magnetic local times are plotted as spatial reference. Red field lines correspond to noon and purple field lines are dusk. As shown in the images, strong ring current emissions

(RCEs) are seen on the nightside near dawn. In addition, there are low-altitude emission (LAE) seen at the Earth rim. The LAE mainly comes from multiple charge exchange and electron stripping processes of energetic ions with the oxygen exosphere [*Roelof*, 1997; *Bazell et al*., 2010; *Buzulukova et al*., 2013].

The RCE at high altitude is produced by ring current ions that charge exchange with the H exosphere [*Roelof and Williams*, 1988; *Fok et al*., 2003]. The local time distribution of the storm time ENA displayed in Figures 3a and 3b is consistent with previous observations and simulation studies [*C:son Brandt et al*., 2002; *Fok et al*., 2003, 2010; *Buzulukova et al*., 2010]. It has been suggested that the post-midnight peak of ENA flux is a result of eastward skewing of the convection potential on the nightside, which is, in turn, a combined effect of ring current shielding electric field and sharp gradient of ionospheric conductance at the terminator [*Fok et al*., 2003; *Ebihara and Fok*, 2004]. CIMI considers the electric coupling between the ring current and ionosphere and is therefore able to capture the skewing of the electric potential and the postmidnight enhancement of ion flux. We have performed a standard CIMI run of the 5–9 April 2010 event (Run 1). In Figures 3c–3e, the CIMI equatorial flux of 20 keV H^+, synthetic ENA images based on the calculated ion flux as viewed by TWINS 1 and 2 are displayed. CIMI predicts strong 20 keV H^+ flux in the post midnight sector at ~18 UT on 6 April 2010. The corresponding ENA emissions resemble the spatial features of the RCE in the TWINS images. There is no LAE in the CIMI ENA because we do not consider ion charge exchange with the O exosphere in this simulation. We plan to include oxygen atoms in our ENA calculation in future studies.

To examine the effects of self-consistent electric (SCE) field on ring current dynamics and development, we perform another CIMI run without the feedback of ring current on ionospheric potential (Run 2). Instead, the empirical model of Weimer [*Weimer*, 2001] is used to specify the potentials in the CIMI domain. Figure 3f shows the equatorial flux of 20 keV H^+ calculated with the Weimer electric field. The peak flux is in the premidnight sector and the intensity is lower than that calculated by SCE (Figure 3c). The corresponding synthetic ENA emission as viewed at the locations of TWINS 1 and 2 are shown in the Figures 3g and 3h. Strong emissions are seen on the nightside toward dusk. When compared with TWINS data (Figures 3a and 3b), the run with SCE reproduces the local time distribution of 20 keV ring current ions much better than the simulation with the empirical Weimer model. We have demonstrated that self-consistent treatment of the currents and electric field in the M-I system is very important to understand the dynamics and development of the storm time ring current.

We note that the color scale for CIMI ENA flux is different from that of the TWINS images. The CIMI ENA flux is higher than that observed. Several factors may contribute to this discrepancy. First, there may be calibration issues in converting TWINS counts to flux. When comparing the ion intensities from deconvolved TWINS images with in situ measurements from the THEMIS satellites, *Grimes et al*. [2013] found that ion fluxes from TWINS were at least three times lower than the THEMIS ion fluxes. Second, the CIMI calculation presented here is performed in the T04 empirical magnetic field model. Without magnetic coupling between the ring current and the global magnetosphere, we may overestimate the buildup of the ring current [*Zaharia et al*., 2006; *Jordanova et al*., 2010]. This problem will be resolved when CIMI is coupled with global MHD models. We have successfully coupled the CRCM with the Block Adaptive Tree Solar wind Roe Upwind Scheme (BATSRUS) MHD model [*Glocer et al*., 2013a; *Meng et al*., 2013]. It should be very straightforward to couple CIMI with BATSRUS or other MHD models. There are additional factors that may cause a stronger ring current: imperfect model of the ionospheric conductance and omission of loss processes, such as interactions with electromagnetic ion cyclotron (EMIC) waves and magnetic field line curvature scattering [*Young et al*., 2008; *Ebihara et al*., 2011]. All these processes will be considered as part of our model improvement.

3.3. CIMI Results Compared With Akebono Data

The Akebono satellite observed enhancements of radiation belt electrons during the active period on 5–9 April 2010. Akebono was launched in February 1989 by the Institute of Space and Astronautical Science in Japan. In April 2010, Akebono was in a high-inclination, highly elliptical orbit with apogee at 5110 km altitude, perigee altitude at 145 km, and orbit period of 2.4 h. The radiation monitor measured electron fluxes in three energy channels: 0.30–0.95 MeV, 0.95–2.5 MeV, and >2.5 MeV [*Takagi et al*., 1993]. Figure 4a shows the *L*-time plot of Akebono electron flux of $E > 2.5$ MeV on 5–9 April 2010. The data have been averaged over six orbits. The *Dst* index is overlaid on the plot. During the main phase of the storm,

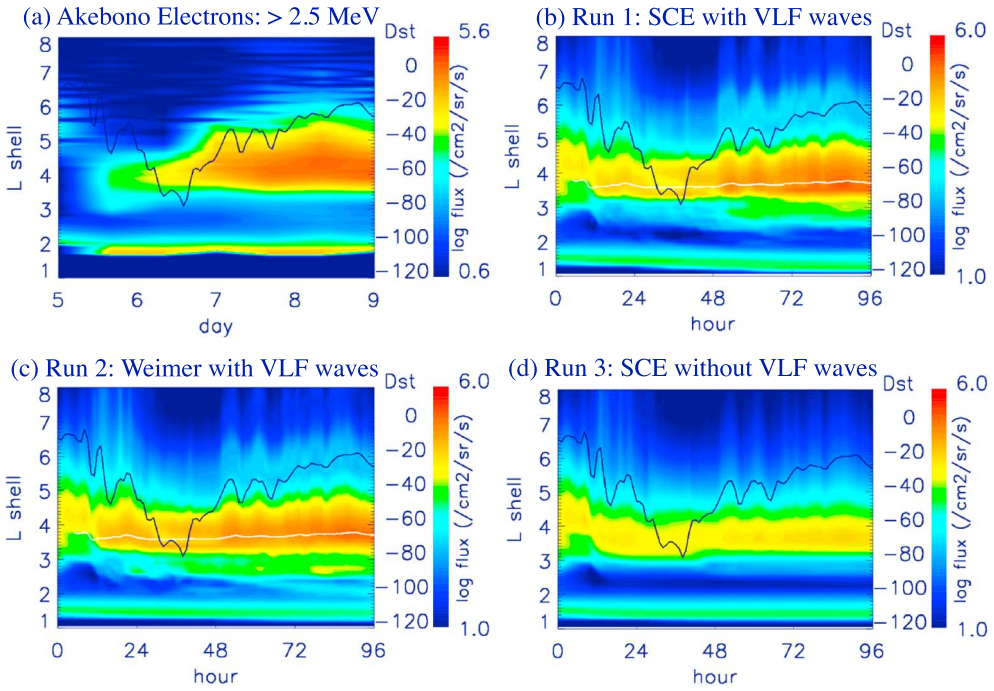

Figure 4. Comparison of Akebono data with CIMI simulated fluxes: (a) *L*-time plot of Akebono electron flux (>2.5 MeV) from 00 UT 5 April to 00 UT 9 April 2010 and simulated fluxes from (b) Run 1, (c) Run 2, and (d) Run 3. The blue curve is the *Dst* index. White curves in Run 1 and Run 2 are calculated plasmapause location.

relativistic electron fluxes are depleted at high *L* ($L > 5$). On the other hand, fluxes start to increase near the peak of the storm at *L* shell around 4. The enhancement continues throughout the recovery phase. On 8 April, fluxes are 2 orders of magnitude higher than the pre-storm level and strong fluxes are seen at $3.5 < L < 5$. In order to understand the mechanisms responsible for the flux dropout at high *L* during the main phase and enhancement in the outer belt during storm recovery, we compare the Akebono data with relativistic electron fluxes at the equator calculated from CIMI runs with different model setups. Even though the CIMI fluxes in Figure 4 are not fluxes at high latitudes as the Akebono data, it has been shown that the temporal variability of low-altitude fluxes is nearly identical with the equatorial fluxes especially during geomagnetic storms [*Kanekal et al.*, 2001, 2005]. In addition to the two runs described in section 3.2, a third run (Run 3) was carried out. Run 3 is the same as Run 1 except no diffusion by chorus and hiss (VLF) waves were considered.

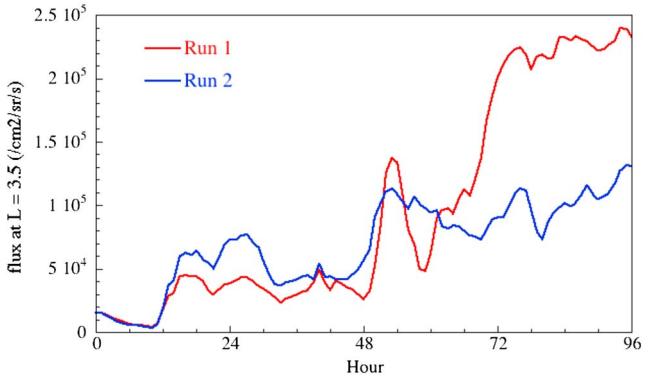

Figure 5. Relativistic (>2.5 MeV) electron flux at $L = 3.5$ calculated from Run 1 (red) and Run 2 (blue).

The *L*-time plots of the CIMI calculated relativistic electron fluxes are posted side by side with the Akebono data in Figure 4. The CIMI equatorial fluxes are displayed with a different color scale than the Akebono flux. The white curves are the minimum plasmapause location at density of 20 cm^{-3}. The prestorm flux from CIMI is relatively higher than the observed because the empirical model of AE8 [*Vette*, 1991; *Fung*, 1996] is used for the initial condition. The AE8 model may not reflect the actual intensity of the relativistic electrons on 5 April. Our emphasis, however, is on the temporal

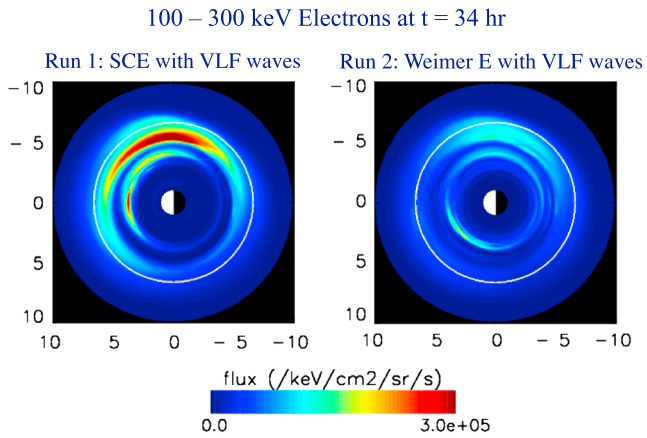

Figure 6. Equatorial flux of 100–300 keV electrons simulated by (left) Run 1 and (right) Run 2 at $t = 34$ h (10:00 UT on 6 April 2010). Sun is on the left in both plots.

variations of the outer belt during this active period. The level of prestorm flux is not the focus in this study. As shown in Figure 4b, the flux dropout at high L ($L > 6$) during the main phase and flux increase in the outer belt seen from the Akebono data are reproduced by the standard CIMI run (Run 1). The flux enhancement mostly takes place outside the plasmapause, consistent with the observation reported by *Li et al.* [2006].

The simulation result of the second CIMI run (Run 2) is displayed in Figure 4c. In this run, the empirical electric field from Weimer [*Weimer*, 2001] is applied to the entire CIMI domain. We have demonstrated in section 3.2 that SCE has significant effect on the spatial distribution of ring current ions (see Figure 3). For radiation belt particles, however, it is commonly believed that their transport is primarily controlled by radial diffusion, and convection should have little effect. As shown in Figure 4c, Run 2 produces both the flux dropout at high L during storm main phase and the enhancement in the outer belt in the recovery phase of the storm as does Run 1 (Figure 4b). Run 2, however, predicts higher relativistic electron flux in the slot region and weaker enhancement in the outer belt in the recovery phase. The relativistic electron flux near the plasmapause from Run 2 at late recovery is noticeably lower than that from Run 1. When compared with the Akebono data, Run 2 is inferior compared to Run 1 in reproducing the strong flux enhancement on 7–9 April 2010. Figure 5, extracted from Figure 4, is a quantitative comparison of >2.5 MeV electron flux at $L = 3.5$ from Run 1 and Run 2. Relativistic electron flux from Run 1 rises rapidly at 60–72 h and reaches a value that is about two times of the flux predicted by Run 2.

The simulation result of the third CIMI run (Run 3) is displayed in Figure 4d. In this run, no wave diffusion from interacting with VLF waves is included and there is only slight flux increase in the outer belt during storm recovery. This run confirms the fact that enhancement of relativistic electron flux seen on 7–9 April is mainly from interacting with VLF waves and, in particular, from energy diffusion by whistler mode chorus waves [*Summers et al.*, 2002; *Horne and Thorne*, 2003; *Horne et al.*, 2005; *Fok et al.*, 2008].

To further investigate why Run 1 produces higher relativistic electron flux, we plot in Figure 6 the equatorial flux of 100–300 keV electrons near the peak of the storm at $t = 34$ h, corresponding to 10:00 UT on 6 April 2010. Figure 6 shows the simulated flux from Run 1 (left) and from Run 2 (right). As shown in the figure, the ring current electron flux from Run 1 is higher than that of Run 2. In Run 1, the consideration of M-I coupling results in a strong convection field in the postmidnight sector, which pushes electrons earthward and energizes them at the same time. These enhanced ring current electrons serve as a seed population for chorus wave energization to the MeV energy range. As a consequence, Run 1 predicts stronger MeV electrons than Run 2, in which the Weimer electric field is applied (Figure 4).

4. Ionospheric Precipitation Predicted by CIMI

As we have illustrated in Figure 1, CIMI outputs electron and ion fluxes in the magnetosphere, as well as precipitating fluxes into the ionosphere. Equation (1) includes multiple processes of different timescales. We use the method of fractional step or operator splitting to decompose the equation and solve only one term at a fractional step [*LeVeque*, 2002; *Fok et al.*, 1993]. We record the differences in distribution functions after each fractional step to obtain the spatial and spectral changes of ion and electron distribution due to each physical process [*Fok et al.*, 2011b]. To calculate the energy flux and mean energy of ionospheric precipitation, we divide particles into 16 energy bins and keep track of the number of particles moving into the loss cone at each energy bin. Figure 7 shows the energy flux and mean energy of precipitating electrons at the ionosphere calculated from Run 1 (Figures 7a, 7c, and 7e) and Run 2 (Figures 7b, 7d, and 7f)

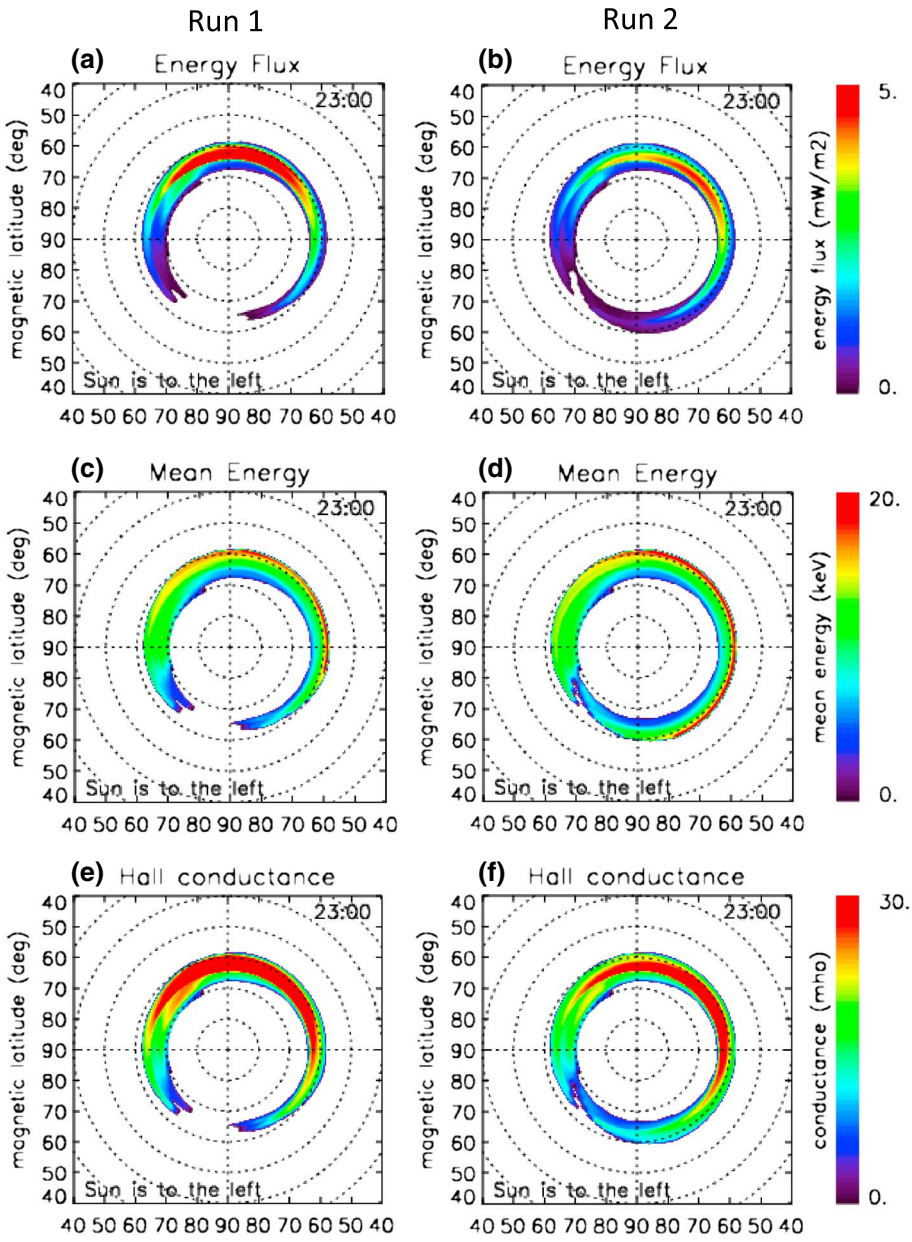

Figure 7. (a and b) Simulated precipitating energy flux, (c and d) mean energy, and (e and f) Hall conductance from Run 1 and Run 2. Only electrons of 0.5 – 30 keV are included in the calculations.

at 23 UT on 5 April during the main phase of the storm. The Sun is on the left in each plot. Only electrons with energy from 0.5 to 30 keV are considered in the calculation which is, in fact, the range that carries most of the precipitating energy and contributes to the conductances in the *F* and *E* regions [*Robinson et al.*, 1987]. As shown in Figures 7a and 7b, the peak precipitation is located at 60°–70° magnetic latitude at postmidnight to dawn local time. The precipitating energy flux from Run 3 without wave diffusion (not shown) is ~2 orders of magnitude lower than those in Run 1 and 2. This difference demonstrates that the precipitation seen in Runs 1 and 2 is mainly from electrons diffused into the loss cone by whistler mode chorus and hiss waves.

The precipitation depicted in Figure 7 shows stronger energy flux from Run 1 and the peak is located more toward dawn than in Run 2. As mentioned in section 3.2, the self-consistent convection field in Run 1 yields an eastward skewing of electric potential that pushes particles toward dawn. The chorus wave power is

also found highest at dawn [*Meredith et al*., 2012]. As a result, Run 1 predicts strong precipitation at dawn. Runs 1 and 2 produce similar mean energy of precipitating electrons (Figures 7c and 7d). The mean energy is higher on the nightside at the equatorial edge of the precipitation region near 60° MLAT, where field lines map to ~4.5 R_E at the equator. When examining the simulated equatorial flux from Run 1, we find electrons with energies higher than 20 keV penetrate deep into 4.5 R_E on the nightside during the period of strong convention around 23 UT on 5 April. As a result, the mean energy of both trapped and precipitating electron flux is higher there.

As shown in Figure 7a, the CIMI model predicts an intensity of electron precipitation on the order of 5 mW/m^2, which corresponds to 5×10^{11} eV/cm^2/s/sr. This energy flux is consistent with the statistical model of *Sotirelis and Newell* [2000]. We derive the Hall conductivity with the simulated energy flux and mean energy using the formula given by *Robinson et al*. [1987]. The results are depicted in Figures 7e and 7f. We obtain the peak Hall conductance in the range of 20–30 mho and strong conductance extends from midnight to dawn. Both the magnitude and the local time distribution of the calculated conductance agree well with the Hardy model [*Hardy et al*., 1987]. Again we have shown that CIMI provides a very good representation of the transport, energization, and precipitation of energetic electrons in the magnetosphere-ionosphere region.

5. Identifying Energization and Loss Mechanisms With CIMI

There have been extensive studies and discussions about what mechanisms are responsible for ring current and radiation belt enhancement and loss during geomagnetic active periods. Strong convection transporting ions and electron from the plasma sheet is believed to be the main cause of ring current buildup in the storm main phase [i.e., *Chen et al*., 1993; *Fok et al*., 1996, 2011b; *Ebihara et al*., 2005]. *Fok et al*. [1999] found that during storm time substorms, the combination of large-scale convection and substorm inductive electric field can push ring current particles to lower L than during steady convection or an isolated substorm. Charge exchange loss was found to be the major loss mechanism during the recovery of the ring current [*Hamilton et al*., 1988; *Fok et al*., 1991; *Jordanova et al*., 1996]. *Liemohn et al*. [1999, 2001], however, suggested that drift-out loss at the dayside magnetopause is the dominant decay process of the ring current, especially during the early recovery phase. For radiation belt electrons, there is ongoing controversy about the balance between energization processes, such as radial and wave diffusion, and loss at the magnetopause [e.g., *O'Brien et al*., 2003; *Horne et al*., 2006; *Ukhorskiy et al*., 2006; *Reeves et al*., 2011; *Baker et al*., 2005; *Nagai*, 2012; *Turner et al*., 2012; *Yu et al*., 2013; *Kim et al*., 2008, 2010, 2011; *Saito et al*., 2010; *Ohtani et al*., 2009].

As mentioned in section 4, we record the differences in distribution functions after each fractional step to obtain the spatial and spectral changes of ion and electron distributions due to each physical process. In calculating particle gain/loss from drift in/out, for each grid cell along the model boundary, the change of distribution function in each time step is determined by

$$\Delta f_s = c_i f_i - c_o f_o \tag{5}$$

where c_i and c_o are the Courant number at the inner and outer boundary of the grid cell, respectively, and f_i and f_o are the corresponding interface values. Particle gain/loss is given by $c_o f_o$. There is a gain if c_o is negative and vice versa. The total particle gain/loss is obtained by integrating $c_o f_o$ over the velocity space and over all boundary grid cells. To calculate the energy gain/loss across the model boundary, we weight the integration by the energy of each differential element in the velocity space. With a similar technique, Δf_s and thus energy changes from drift, charge exchange, wave diffusion, and precipitation at the loss cone can be estimated. This capability can shed new light on the sources of radiation belt and ring current enhancement and loss. Figure 8 shows the accumulated energy changes due to various processes during the storm on 5–9 April 2010 for ring current H^+ (1–300 keV, Figures 8(1a)–8(1d)), ring current electrons (1–300 keV, Figures 8(2a)–8(2d)) and radiation belt electrons (0.3–5 MeV, Figures 8(3a)–8(3d)). Figures 8(1a), 8(2a), and 8(3a) display energy changes in the entire simulation domain at $1 < L < 9$. The total energy contents of each plasma population are shown in black curves. The lower 3 panels exhibit energy gain/loss in three subregions: ($1 < L < 3$) inner ring current, inner belt, and slot region; ($3 < L < 5$) peak ring current and peak outer belt; and ($5 < L < 9$) outer ring

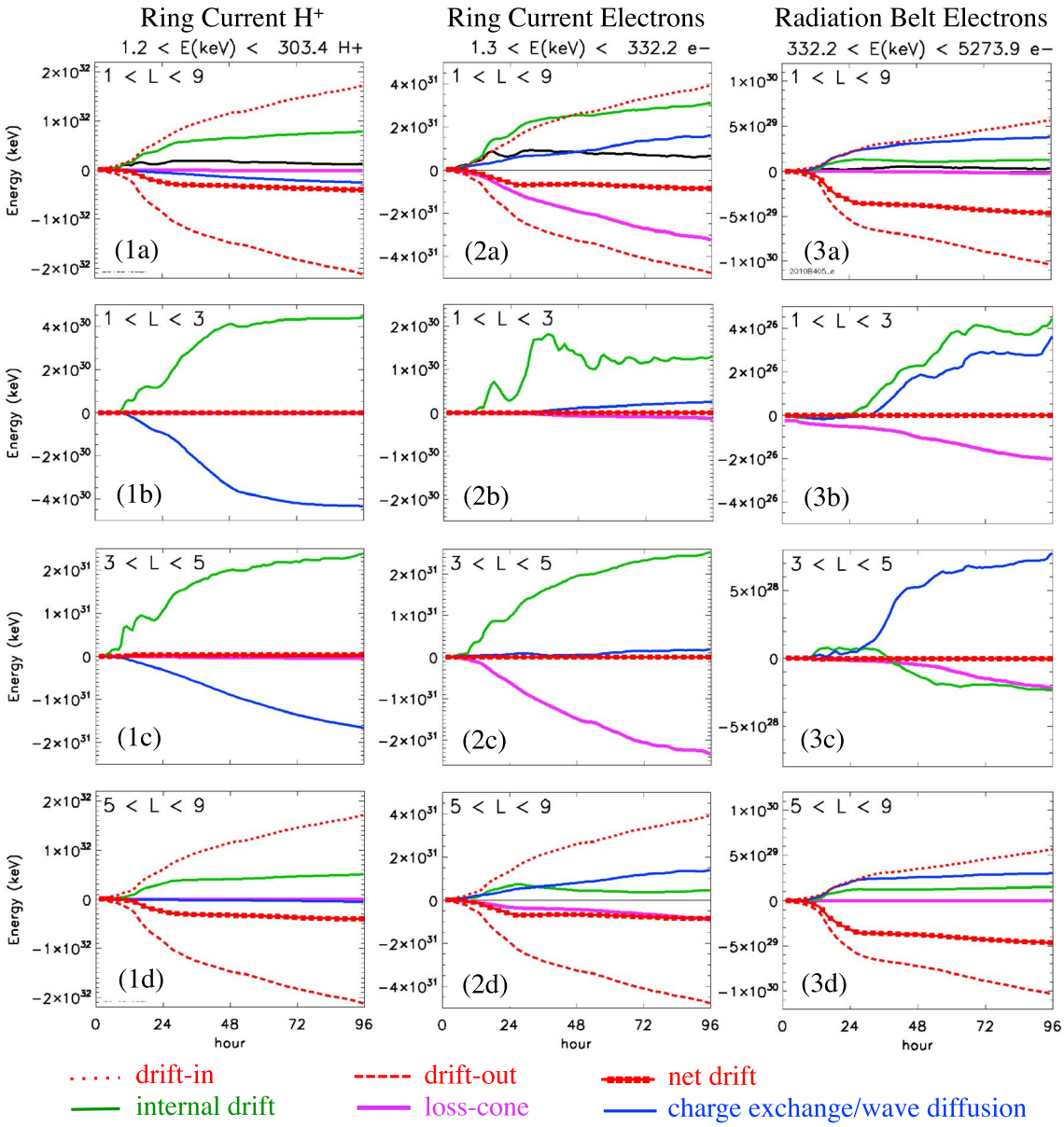

Figure 8. Contribution of individual processes to the total energy content (black curves) in ring current H^+ (1a–1d), (2a–2d) ring current electrons, and (3a–3d) radiation belt electrons during the storm on 5–9 April 2010. Red dotted/dashed lines are accumulated energy gain/loss from particle drift in/out from the CIMI domain. Red curves with squares are net change from drift in and drift out. The green lines are energy changes from internal transport. The thick purple lines are losses at the loss cone. The blue lines are charge exchange loss for ions and changes from wave diffusion for electrons.

current and outer part of the outer belt. In each plot, red dotted/dashed lines represent accumulated energy gain/loss from particle drift in/out from the CIMI domain. The red curves with squares are net change from drift in and out the model boundary. The green lines are energy changes due to adiabatic acceleration or deceleration from internal transport, which is obtained by subtracting the total change from drift with net gain/loss from drifting across the model boundary. The thick purple lines represent losses into the loss cone. The blue lines are charge exchange loss for ions and changes from wave diffusion for electrons. Other than the black curves of total energy content, all curves in Figure 8 are accumulated changes. The rate of energy variation at a given time due to each process can be inferred from the slope of the curve at that particular time. Note that the scales of the plots in Figure 8 are not the same.

Much important information on the causes of ring current and radiation belt variations can be gathered from the analysis shown in Figure 8. One can clearly identify the dominant process at different regions of the inner magnetosphere at different phases of the storm. As shown in Figure 8(1a), the major process in the buildup of the ring current ions is particle energization from strong convection (green curve). The dominant loss process is drift loss (red line with squares) at the boundary or the magnetopause. Charge exchange loss (blue curve) is significant but less important than the drift loss. For this simulation, no wave diffusion is considered for ions, so the loss into the loss cone (thick purple curve) is only by drift motion and the loss is minimal. Figure 8(1b) shows that, at $1 < L < 3$, convection energization is counteracted by charge exchange loss. The gain/loss rates of these two processes decrease significantly during the storm recovery at $t > 48$ h since H^+ have diminished greatly in the inner region by that time. In contrast, charge exchange loss rate at $3 < L < 5$ (Figure 8(1c)) is relatively steady throughout the storm, although it is surpassed by adiabatic acceleration. For this particular event, drift gain/loss happens only at $L > 5$ (Figure 8(1d)). Ring current ions are drifting in and out from early main phase to late recovery. During the main phase, loss at the magnetopause exceeds the influx from the plasma sheet, resulting in a net loss of particles and energy. The drift in and drift out are pretty much balanced during the recovery phase. In this outer part of the ring current, convection energization is dominant over losses. Charge exchange is weak because neutral density is low here.

Figure 8(2a) shows the major energization and loss mechanisms of ring current electrons. The primary energization for ring current electrons is from adiabatic transport (green line) just as it is for the ring current ions. Ring current electrons, however, are lost mainly by loss into the loss cone (thick purple line). Electrons are diffused into the loss cone by whistler mode chorus waves and plasmaspheric hiss. These pitch angle diffusion processes are most intense at $3 < L < 5$ (Figure 8(2c)), the nominal location of the plasmapause [*Carpenter and Anderson*, 1992; *Gallagher et al*., 1995; *Moldwin et al*., 2002]. Electrons are diffused into the loss cone by hiss waves inside the plasmapause and diffused by chorus waves outside this plasmasphere boundary [i.e., *Summers et al*., 2007]. Another energization process of ring current electrons is diffusion with plasma waves at $5 < L < 9$ (Figure 8(2d), blue curve). Since only energy diffusion changes particle energy content and only chorus waves are assumed in this large L region, this enhancement is a result of energy diffusion by chorus waves. The increase in electron energy is larger than the loss from pitch angle diffusion with the same wave mode (Figure 8(2d), thick purple curve). To understand why the relative effects of chorus wave pitch angle scattering and energy diffusion on ring current electrons switch from $3 < L < 5$ to $5 < L < 9$, we examine how the diffusion coefficients ($D_{\alpha\alpha}$ and D_{EE}) vary with location. In the vicinity just outside the plasmapause, the ratio of plasma frequency to the cyclotron frequency (f_{pe}/f_{ce}) is relatively low with the value of ~4 [*Fok et al*., 2008]. The ratio increases with increasing L from the plasmapause. At $f_{pe}/f_{ce} < 5$, $D_{\alpha\alpha}$ for 100 keV electrons is large for a wide range of pitch angles [*Albert*, 2005; *Horne et al*., 2006]. As a result, electrons experience strong pitch angle diffusion near the plasmapause. At larger L where f_{pe}/f_{ce} is high, both D_{EE} and $D_{\alpha\alpha}$ are decreased, especially at small pitch angles. It takes a long time to push electrons into the loss cone of small pitch angles. The relatively strong energy diffusion at large pitch angles, however, accelerates perpendicular particles and increases the overall electron energy (Figure 8(2d)). During the main phase of the storm, the net drift loss of ring current electrons (Figure 8(2a), red curve with squares) is comparable with the precipitation loss (Figure 8(2a), thick purple curve). The drift loss, however, ceases in the storm recovery while pitch angle diffusion continues steadily throughout the storm.

Figures 8(3a)–8(3d) display the energy budget for radiation belt electrons. As shown in Figure 8(3a), energy diffusion by plasma waves (blue curve) is the dominant acceleration process. For relativistic electrons, energy diffusion is more effective than pitch angle diffusion at all L ranges (Figures 8(3b)–8(3d), blue and thick purple curves). Overall, adiabatic transport (Figures 8(3a)–8(3d)) accelerates relativistic electrons in the radiation belts, except at $3 < L < 5$, at $30 < t < 60$ h when *Dst* is strongly negative (Figure 8(3c), times of negative slope of green curve). This loss of particle energy during strong *Dst* is consistent with the well-known *Dst* effect [*Dessler and Karplus*, 1961; *Kim and Chan*, 1997]. The magnetic field produced by the ring current inflates the main field. The drift shells of energetic particles in the radiation belt expand outward correspondingly (conservation of the third adiabatic invariant) and particles decelerate. Our simulation implies that, for this event, the *Dst* effect produces permanent loss at the heart of the outer belt as the green curve in Figure 8(3c) shows no recovery after the decrease. We suggest that as the drift shells of electrons expand outward, they intercept the magnetopause, causing irreversible drift loss. Net loss at the model boundary is the major loss

Table 1. Dominant Energization and Loss Processes and Their Locations of Ring Current H^+, Electrons, and Radiation Belt Electrons

	Plasma Population		
Dominant process	Ring current H+	Ring current electron	Radiation belt electron
Energization (L shells)	Adiabatic transport ($5 < L < 9$)	Adiabatic transport ($3 < L < 5$)	Energy diffusion by chorus ($5 < L < 9$)
Loss (L shells)	Drift loss ($5 < L < 9$)	Pitch angle diffusion by chorus ($3 < L < 5$)	Drift loss ($5 < L < 9$)

mechanism for relativistic electrons as shown by the red curve with squares in Figure 8(3d). The loss is the strongest during the storm main phase when the magnetopause standoff distance is small. In Table 1, we summarize, for this event, the dominant energization and loss processes and where they take place for radiation belt electrons and ring current ions and electrons.

6. Discussion and Conclusions

We have demonstrated the unprecedented capabilities of the CIMI model. As demonstrated in Figure 1, CIMI calculates the 3-D distributions of energetic ions, electrons, and cold plasma in the inner magnetosphere and, self-consistently, the electric currents and field and particle precipitation in the ionosphere. CIMI is thus a powerful tool for studying the dynamics of the ring current, radiation belts, and plasmasphere along with how they respond to solar wind input and their couplings with the ionosphere. In the simulations shown in this paper, the Tsyganenko 2004 magnetic field model was used; however, it should be straightforward to incorporate CIMI with MHD models. This type of code merging has been done with CIMI's predecessors: CRCM and RBE [e.g., *Glocer et al.*, 2011, 2013a].

The unique features and capabilities of the CIMI model are highly relevant to the Van Allen Probes (RBSP) mission. One of the scientific objectives of the RBSP mission is to understand and quantify the loss of radiation belt electrons and determine the balance between competing acceleration and loss processes. The analysis we presented in the last section is extremely useful in identifying the roles and location of different energization and decay mechanisms. We have modeled an RBSP event in November 2012 using the BATSRUS-CRCM model [*Glocer et al.*, 2013b]. On 14 November 2012, RBSP observed significant ion and electron flux dropouts at ring current and radiation belt energies. We simulated this event and extracted simulated magnetic field and ring current ion fluxes along the RBSP trajectories for direct comparison with the observations. We found that ring current pressure feedback is essential to capturing the observed dropouts. Strong pressure from the

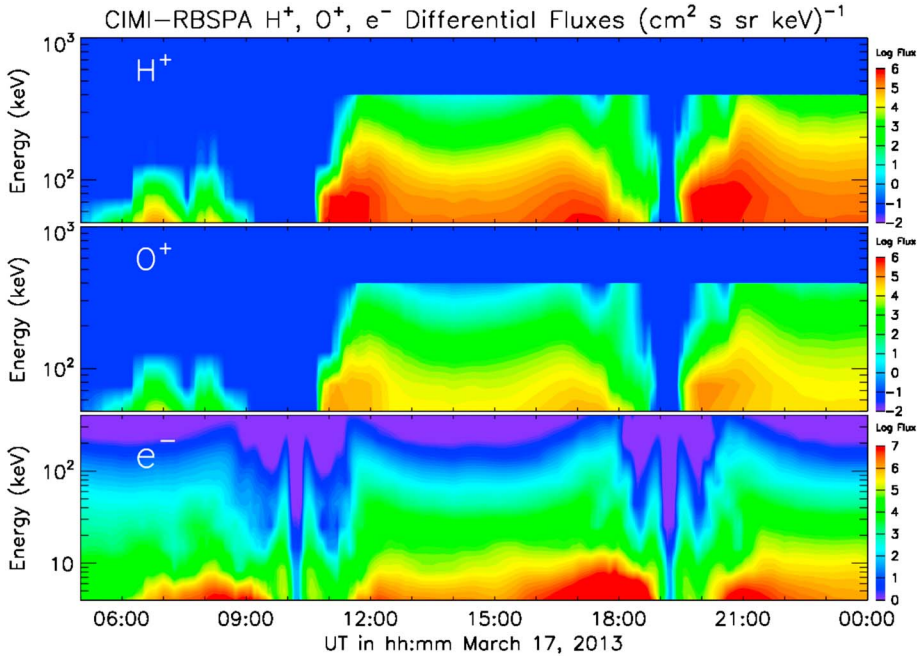

Figure 9. CIMI simulated fluxes along the RBSP-A orbit on 17 March 2013: (top) H^+, (middle) O^+, and (bottom) electrons.

ring current stretched the field lines so that RBSP satellites were connected to the lobe region where energetic particle fluxes are low. The CIMI model is now available for "Runs on Request" at the Community Coordinated Modeling Center (CCMC; http://ccmc.gsfc.nasa.gov). Figure 9 shows the CIMI pitch angle averaged flux of ions and electrons extracted along the RBSP-A orbit during the main phase of the storm on 17 March 2013. Figure 9 shows energy-time spectrograms of (top) H^+ and (middle) O^+ and (bottom) for electrons. The ion energies match those of the Radiation Belt Storm Probes Ion Composition Experiment instrument [*Mitchell et al*., 2013], and the electron flux is in the Energetic Particle Composition and Thermal Plasma Suite - Magnetic Electron Ion Spectrometer energy range [*Spence et al*., 2013]. CIMI reproduces the rapid increase of ion and electron fluxes at ~06 UT at the storm sudden commencement and the subsequent enhancement throughout the main phase.

The CIMI model described above forms a framework of global modeling of the inner magnetosphere and ionosphere. Additional features and improvement can easily be implemented into the model. We plan to include EMIC wave diffusion in ring current ions and radiation belt electrons. A combined theoretical-empirical treatment for EMIC waves will be applied. The local EMIC growth rate will be estimated by the ring current ion anisotropy calculated from CIMI [*Kozyra et al*., 1984, 1997; *Jordanova et al*., 1997]. The EMIC wave amplitude can be, in turn, estimated by the growth rate following the approach of *Bortnik et al*. [2011]. Another model advancement is to update our auroral conductance with simulated ion and electron precipitations. We have shown in Figure 7 that CIMI produces observable ionospheric precipitation and the corresponding conductance. With the self-consistent treatment of conductance and electric field, we are able to study the response and modulation of the ionosphere to processes happening in the magnetosphere, in this case, particle pitch angle diffusion into the loss cone.

In summary, a Comprehensive Inner-Magnetosphere-Ionosphere (CIMI) model has been developed to understand the physical processes controlling the dynamics of magnetospheric plasmas and their coupling with the ionosphere electric current and field. To date the findings from this model development work include the following:

1. In modeling the storm on 5–9 April 2010 with empirical electric field and self-consistent electric field with M-I coupling, we found that the latter produces stronger electron seed population for wave acceleration to relativistic energy.
2. The dominant energization process for ring current ions and electrons is adiabatic acceleration and, for more energetic radiation belt electrons, energy diffusion by whistler mode chorus waves.
3. Drift loss is the major loss mechanism for ring current ions and radiation belt electrons. Ring current electron decay is mainly caused by pitch angle diffusion due to chorus waves. The corresponding electron loss can account for the observed precipitation in the ionosphere.
4. CIMI is a powerful tool for analyzing and interpreting data from the RBSP mission. CIMI is available to the community at CCMC for "Runs on Request."

Acknowledgments

The authors thank Donald Fairfield for many valuable comments. We thank ACE, WIND, and OMNI teams for providing solar wind data through Space Physics Data Facility of NASA Goddard Space Flight Center. The *AL*, *AU*, *Dst* and *SYM-H* indices are provided by Kyoto University World Data Center for Geomagnetism. We also gratefully acknowledge Jay Albert of Air Force Research Laboratory for providing the VLF wave diffusion coefficients. The TWINS data shown in this paper were downloaded at the TWINS website at http://twins.swri.edu. To access the Akebono data, contact Tsugunobu Nagai at nagai@geo.titech.ac.jp. This work was supported by the TWINS mission as a part of NASA's Explorer Program, and by NASA Heliophysics Living With a Star Targeted Research and Technology program, under Work Breakdown Structure 936723.02.01.09.47. Part of the research in this paper was supported by Van Allen Probes mission funding.

Michael Liemohn thanks Dae-Young Lee and another reviewer for their assistance in evaluating the paper.

References

Acuna, M. H., K. W. Ogilvie, D. N. Baker, S. A. Curtis, D. H. Fairfield, and W. H. Mish (1995), The global Geospace program and its investigation, *Space Sci. Rev.*, *71*, 5–21.

Albert, J. M. (2005), Evaluation of quasi-linear diffusion coefficients for whistler mode waves in a plasma with arbitrary density ratio, *J. Geophys. Res.*, *110*, A03218, doi:10.1029/2004JA010844.

Albert, J. M. (2008), Efficient approximations of quasi-linear diffusion coefficients in the radiation belts, *J. Geophys. Res.*, *113*, A06208, doi:10.1029/2007JA012936.

Albert, J. M., N. P. Meredith, and R. B. Horne (2009), Three-dimensional diffusion simulation of outer radiation belt electrons during the 9 October 1990 magnetic storm, *J. Geophys. Res.*, *114*, A09214, doi:10.1029/2009JA014336.

Angelopoulos, V. (2008), The THEMIS mission, *Space Sci. Rev.*, *141*, 5–34.

Baker, D. N., W. Aiello, J. R. Asbridge, R. D. Belian, P. R. Higbie, R. W. Klebesadel, J. G. Laros, and E. R. Tech (1985), Los Alamos energetic particle sensor systems at geostationary orbit, *AIAA 85–0243*, New York.

Baker, D. N., G. M. Mason, O. Figueroa, G. Colon, J. G. Watzin, and R. M. Aleman (1993), An overview of the Solar, Anomalous, and Magnetospheric Particle Explorer (SAMPEX) mission, *IEEE Trans. Geosci. Remote Sens.*, *31*, 531–541.

Baker, D. N., S. R. Elkington, X. Li, and M. J. Wiltberger (2005), Particle acceleration in the inner magnetosphere, in *The Inner Magnetosphere: Physics and Modeling*, *Geophys. Monogr. Ser.*, vol. 155, edited by T. I. Pulkkinen et al., pp. 73–85, AGU, Washington, D. C.

Baumjohann, W., G. Paschmann, and C. A. Cattell (1989), Average plasma properties in the central plasma sheet, *J. Geophys. Res.*, *94*, 6597–6606, doi:10.1029/JA094iA06p06597.

Bazell, D., E. Roelof, T. Sotirelis, P. C. Brandt, H. Nair, P. Valek, J. Goldstein, and D. McComas (2010), Comparison of TWINS images of low-altitude emissions of energetic neutral atoms with DMSP precipitating ion fluxes, *J. Geophys. Res.*, *115*, A10204, doi:10.1029/2010JA015644.

Borovsky, J. E., and M. H. Denton (2006), Differences between CME-driven storms and CIR-driven storms, *J. Geophys. Res.*, *111*, A07S08, doi:10.1029/2005JA011447.

Borovsky, J. E., M. F. Thomsen, and R. C. Elphic (1998), The driving of the plasma sheet by the solar wind, *J. Geophys. Res.*, *103*, 17,617–17,639, doi:10.1029/97JA02986.

Bortnik, J., N. Omidi, L. Chen, R. M. Thorne, and R. B. Horne (2011), Saturation characteristics of electromagnetic ion cyclotron waves, *J. Geophys. Res.*, *116*, A09219, doi:10.1029/2011JA016638.

Buzulukova, N., M.-C. Fok, T. E. Moore, and D. M. Ober (2008), Generation of plasmaspheric undulations, *Geophys. Res. Lett.*, *35*, L13105, doi:10.1029/2008GL034164.

Buzulukova, N., M.-C. Fok, J. Goldstein, P. Valek, D. J. McComas, and P. C. Brandt (2010), Ring current dynamics in moderate and strong storms: Comparative analysis of TWINS and IMAGE/HENA data with the Comprehensive Ring Current Model, *J. Geophys. Res.*, *115*, A12234, doi:10.1029/2010JA015292.

Buzulukova, N., M.-C. Fok, E. Roelof, J. Redfern, J. Goldstein, P. Valek, and D. McComas (2013), Comparative analysis of low-altitude ENA emissions in two substorms, *J. Geophys. Res. Space Physics*, *118*, 724–731, doi:10.1002/jgra.50103.

C:son Brandt, P., S. Ohtani, D. G. Mitchell, M. -C. Fok, E. C. Roelof, and R. Demajistre (2002), Global ENA observations of the storm main phase ring current: Implications for skewed electric fields in the inner magnetosphere, *Geophys. Res. Lett.*, *29*(20, 1954), doi:10.1029/2002GL015160.

Carpenter, D. L., and R. R. Anderson (1992), An ISEE/whistler model of equatorial electron density in the magnetosphere, *J. Geophys. Res.*, *97*, 1097–1108, doi:10.1029/91JA01548.

Chen, M. W., M. Schulz, L. R. Lyons, and D. J. Gorney (1993), Storm time transport of ring current and radiation belt ions, *J. Geophys. Res.*, *98*, 3835–3849, doi:10.1029/92JA02608.

Connors, M., C. T. Russell, and V. Angelopoulos (2011), Magnetic flux transfer in the 5 April 2010 Galaxy 15 substorm: An unprecedented observation, *Ann. Geophys.*, *29*, 619–622, doi:10.5194/angeo-29-619-2011.

Denton, M. H., and J. E. Borovsky (2012), Magnetosphere response to high-speed solar wind streams: A comparison of weak and strong driving and the importance of extended periods of fast solar wind, *J. Geophys. Res.*, *117*, A00L05, doi:10.1029/2011JA017124.

Dessler, A. J., and R. Karplus (1961), Some effects of diamagnetic ring currents on Van Allen radiation, *J. Geophys. Res.*, *66*, 2289–2295, doi:10.1029/JZ066i008p02289.

Ebihara, Y., and M. Ejiri (2000), Simulation study on fundamental properties of the storm time ring current, *J. Geophys. Res.*, *105*(15), 15,843–15,859, doi:10.1029/1999JA900493.

Ebihara, Y., and M.-C. Fok (2004), Post-midnight storm time enhancement of ten-of-keV proton flux, *J. Geophys. Res.*, *109*, A12209, doi:10.1029/2004JA010523.

Ebihara, Y., M.-C. Fok, S. Sazykin, M. F. Thomsen, M. R. Hairston, D. S. Evans, F. J. Rich, and M. Ejiri (2005), Ring current and the magnetosphere-ionosphere coupling during the superstorm of 20 November 2003, *J. Geophys. Res.*, *110*, A09S22, doi:10.1029/2004JA010924.

Ebihara, Y., M.-C. Fok, J. B. Blake, and J. F. Fennell (2008), Magnetic coupling of the ring current and the radiation belt, *J. Geophys. Res.*, *113*, A07221, doi:10.1029/2008JA013267.

Ebihara, Y., M.-C. Fok, T. J. Immel, and P. C. Brandt (2011), Rapid decay of storm time ring current due to pitch angle scattering in curved field line, *J. Geophys. Res.*, *116*, A03218, doi:10.1029/2010JA016000.

Fok, M.-C., and T. E. Moore (1997), Ring current modeling in a realistic magnetic field configuration, *Geophys. Res. Lett.*, *24*, 1775–1778, doi:10.1029/97GL01255.

Fok, M.-C., J. U. Kozyra, A. F. Nagy, and T. E. Cravens (1991), Lifetime of ring current particles due to Coulomb collisions in the plasmasphere, *J. Geophys. Res.*, *96*, 7861–7867, doi:10.1029/90JA02620.

Fok, M.-C., J. U. Kozyra, A. F. Nagy, C. E. Rasmussen, and G. V. Khazanov (1993), Decay of equatorial ring current ions and associated aeronomical consequences, *J. Geophys. Res.*, *98*, 19,381–19,393, doi:10.1029/93JA01848.

Fok, M.-C., T. E. Moore, and M. E. Greenspan (1996), Ring current development during storm main phase, *J. Geophys. Res.*, *101*, 15,311–15,322, doi:10.1029/96JA01274.

Fok, M.-C., T. E. Moore, and D. C. Delcourt (1999), Modeling of inner plasma sheet and ring current during substorms, *J. Geophys. Res.*, *104*, 14,557–14,569, doi:10.1029/1999JA900014.

Fok, M.-C., T. E. Moore, and W. N. Spjeldvik (2001a), Rapid enhancement of radiation belt electron fluxes due to substorm dipolarization of the geomagnetic field, *J. Geophys. Res.*, *106*, 3873–3881, doi:10.1029/2000JA000150.

Fok, M.-C., R. A. Wolf, R. W. Spiro, and T. E. Moore (2001b), Comprehensive computational model of the Earth's ring current, *J. Geophys. Res.*, *106*, 8417–8424, doi:10.1029/2000JA000235.

Fok, M.-C., et al. (2003), Global ENA IMAGE simulations, *Space Sci. Rev.*, *109*, 77–103.

Fok, M.-C., Y. Ebihara, T. E. Moore, D. M. Ober, and K. A. Keller (2005), Geospace storm processes coupling the ring current, radiation belt and plasmasphere, in *Inner Magnetosphere Interactions: New Perspectives from Imaging*, *Geophys. Monogr. Ser.*, vol. 159, edited by J. Burch et al., pp. 207–220, AGU, Washington, D. C.

Fok, M.-C., R. B. Horne, N. P. Meredith, and S. A. Glauert (2008), The radiation belt environment model: Application to space weather nowcasting, *J. Geophys. Res.*, *113*, A03S08, doi:10.1029/2007JA012558.

Fok, M.-C., N. Buzulukova, S.-H. Chen, P. W. Valek, J. Goldstein, and D. J. McComas (2010), Simulation and TWINS observations of the 22 July 2009 storm, *J. Geophys. Res.*, *115*, A12231, doi:10.1029/2010JA015443.

Fok, M.-C., A. Glocer, Q. Zheng, R. B. Horne, N. P. Meredith, J. M. Albert, and T. Nagai (2011a), Recent developments in the radiation belt environment model, *J. Atmos. Sol. Terr. Phys.*, *73*, 1435–1443.

Fok, M.-C., T. E. Moore, S. P. Slinker, J. A. Fedder, D. C. Delcourt, M. Nosé, and S.-H. Chen (2011b), Modeling the super storm in November 2003, *J. Geophys. Res.*, *116*, A00J17, doi:10.1029/2010JA015720.

Fung, S. F. (1996), Recent development in the NASA trapped radiation model, in *Radiation Belts: Models and Standards*, *Geophys. Monogr. Ser.*, vol. 97, edited by J. F. Lemaire, D. Heynderickx, and D. N. Baker, pp. 79–91, AGU, Washington, D. C.

Gallagher, D. L., P. D. Craven, R. H. Comfort, and T. E. Moore (1995), On the azimuthal variation of core plasma in the equational magnetosphere, *J. Geophys. Res.*, *100*, 23,597–23,605, doi:10.1029/95JA02100.

Garner, T. W., R. A. Wolf, R. W. Spiro, W. J. Burke, B. G. Fejer, S. Sazykin, J. L. Roeder, and M. R. Hairston (2004), Magnetospheric electric fields and plasma sheet injection to low L-shells during the 4–5 June 1991 magnetic storm: Comparison between the Rice Convection Model and observations, *J. Geophys. Res.*, *109*, A02214, doi:10.1029/2003JA010208.

Gkioulidou, M., C.-P. Wang, S. Wing, L. R. Lyons, R. A. Wolf, and T.-S. Hsu (2012), Effect of an MLT dependent electron loss rate on the magnetosphere-ionosphere coupling, *J. Geophys. Res.*, *117*, A11218, doi:10.1029/2012JA018032.

Glocer, A., G. Toth, M. Fok, T. Gombosi, and M. Liemohn (2009), Integration of the radiation belt environment model into the space weather modeling framework, *J. Atmos. Sol. Terr. Phys.*, doi:10.1016/j.jastp.2009.01.003.

Glocer, A., M.-C. Fok, T. Nagai, G. Tóth, T. Guild, and J. Blake (2011), Rapid rebuilding of the outer radiation belt, *J. Geophys. Res.*, *116*, A09213, doi:10.1029/2011JA016516.

Glocer, A., M. Fok, X. Meng, G. Toth, N. Buzulukova, S. Chen, and K. Lin (2013a), CRCM + BATS-R-US two way coupling, *J. Geophys. Res. Space Physics*, *118*, 1635–1650, doi:10.1002/jgra.50221.

Glocer, A., N. Y. Buzulukova, M.-C. Fok, D. G. Sibeck, and S.-H. Chen (2013b), Multi-physics simulations of Van Allen Probes observations of November 14, 2012, Abstract SM33C-05 presented at 2013 AGU Fall Meeting, San Francisco, Calif., 9–13 Dec.

Goldstein, J., P. Valek, D. J. McComas, and J. Redfern (2012), TWINS energetic neutral atom observations of local-time-dependent ring current anisotropy, *J. Geophys. Res.*, *117*, A11213, doi:10.1029/2012JA017804.

Goldstein, J., P. Valek, D. J. McComas, J. Redfern, and F. Soraas (2013), Local-time dependent low-altitude ion spectra deduced from TWINS ENA images, *J. Geophys. Res. Space Physics*, *118*, 2928–2950, doi:10.1002/jgra.50222.

Grimes, E. W., J. D. Perez, J. Goldstein, D. J. McComas, P. Valek, and D. Turner (2013), Comparison of TWINS and THEMIS observations of proton pitch angle distributions in the ring current during the 29 May 2010 geomagnetic storm, *J. Geophys. Res. Space Physics*, *118*, 4895–4905, doi:10.1002/jgra.50455.

Hamilton, D. C., G. Gloeckler, F. M. Ipavich, W. Studemann, B. Wilken, and G. Kremser (1988), Ring current development during the great geomagnetic storm of February 86, *J. Geophys. Res.*, *93*, 14,343–14,355, doi:10.1029/JA093iA12p14343.

Hardy, D. A., M. S. Gussenhoven, R. Raistrick, and W. J. McNeil (1987), Statistical and functional representations of the pattern of auroral energy flux, number flux, and conductivity, *J. Geophys. Res.*, *92*, 12,275–12,294, doi:10.1029/JA092iA11p12275.

Higbie, P. R., R. D. Belian, and D. N. Baker (1978), High-resolution energetic particle measurements at 6.6 R_E: 1 electron micropulsations, *J. Geophys. Res.*, *88*, 4851–4855, doi:10.1029/JA083iA10p04851.

Horne, R. B., and R. M. Thorne (2003), Relativistic electron acceleration and precipitation during resonant interactions with whistler mode chorus, *Geophys. Res. Lett.*, *30*(10, 1527), doi:10.1029/2003GL016973.

Horne, R. B., R. M. Thorne, S. A. Glauert, J. M. Albert, N. P. Meredith, and R. R. Anderson (2005), Timescale for radiation belt electron acceleration by whistler mode chorus waves, *J. Geophys. Res.*, *110*, A03225, doi:10.1029/2004JA010811.

Horne, R. B., N. P. Meredith, S. A. Glauert, A. Varotsou, D. Boscher, R. M. Thorne, Y. Y. Shprits, and R. R. Anderson (2006), Mechanisms for the acceleration of radiation belt electrons, in *Recurrent Magnetic Storms: Corotating Solar Wind Streams*, *Geophys. Monogr. Ser.*, vol. 167, edited by B. T. Tsurutani et al., pp. 151–173, AGU, Washington, D. C.

Johnson, M. H., and J. K. Ball (1992), Combined Release and Radiation Effects Satellite (CRRES): Spacecraft and mission, *J. Spacecr. Rockets*, *29*(4), 556–563.

Jordanova, V. K., L. M. Kistler, J. U. Kozyra, G. V. Khazanov, and A. F. Nagy (1996), Collisional losses of ring current ions, *J. Geophys. Res.*, *101*, 111–126, doi:10.1029/95JA02000.

Jordanova, V. K., J. U. Kozyra, A. F. Nagy, and G. V. Khazanov (1997), Kinetic model of the ring current-atmosphere interactions, *J. Geophys. Res.*, *102*, 14,279–14,291, doi:10.1029/96JA03699.

Jordanova, V. K., S. Zaharia, and D. T. Welling (2010), Comparative study of ring current development using empirical, dipolar, and self-consistent magnetic field simulations, *J. Geophys. Res.*, *115*, A00J11, doi:10.1029/2010JA015671.

Kanekal, S. G., D. N. Baker, and J. B. Blake (2001), Multisatellite measurements of relativistic electron: Global coherence, *J. Geophys. Res.*, *106*, 29,721–29,732, doi:10.1029/2001JA000070.

Kanekal, S. G., R. Friedel, G. D. Reeves, D. N. Baker, and J. B. Blake (2005), Relativistic electron events in 2002: Studies of pitch angle isotropization, *J. Geophys. Res.*, *110*, A12224, doi:10.1029/2004JA010974.

Kataoka, R., and Y. Miyoshi (2006), Flux enhancement of radiation belt electrons during geomagnetic storms driven by coronal mass ejections and corotating interaction regions, *Space Weather*, *4*, S09004, doi:10.1029/2005SW000211.

Kim, H.-J., and A. A. Chan (1997), Fully relativistic changes in storm time relativistic electron fluxes, *J. Geophys. Res.*, *102*, 22,107–22,116, doi:10.1029/97JA01814.

Kim, K. C., D.-Y. Lee, H.-J. Kim, L. R. Lyons, E. S. Lee, M. K. Ozturk, and C. R. Choi (2008), Numerical calculations of relativistic electron drift loss effect, *J. Geophys. Res.*, *113*, A09212, doi:10.1029/2007JA013011.

Kim, K. C., D.-. Y. Lee, H.-. J. Kim, E. S. Lee, and C. R. Choi (2010), Numerical estimates of drift loss and *Dst* effect for outer radiation belt relativistic electrons with arbitrary pitch angle, *J. Geophys. Res.*, *115*, A03208, doi:10.1029/2009JA014523.

Kim, K.-C., D.-Y. Lee, Y. Shprits, H.-J. Kim, and E. Lee (2011), Electron flux changes in the outer radiation belt by radial diffusion during the storm recovery phase in comparison with the fully adiabatic evolution, *J. Geophys. Res.*, *116*, A09229, doi:10.1029/2011JA016642.

Kozyra, J. U., T. E. Cravens, A. F. Nagy, E. G. Fontheim, and R. S. B. Ong (1984), Effect of energetic heavy ions on electromagnetic ion cyclotron wave generation in the plasmapause region, *J. Geophys. Res.*, *89*, 2217–2233, doi:10.1029/JA089iA04p02217.

Kozyra, J. U., V. K. Jordanova, R. B. Horne, and R. M. Thorne (1997), Modeling of the contribution of electromagnetic ion cyclotron (EMIC) waves to storm time ring current erosion, in *Magnetic Storms*, *Geophys. Monogr. Ser.*, vol. 98, edited by B. T. Tsurutani et al., pp. 187–202, AGU, Washington, D. C.

LeVeque, R. J. (2002), *Finite Volume Methods for Hyperbolic Problems*, Cambridge Univ. Press, New York.

Li, X., D. N. Baker, T. P. O'Brien, L. Xie, and Q. G. Zong (2006), Correlation between the inner edge of outer radiation belt electrons and the innermost plasmapause location, *Geophys. Res. Lett.*, *33*, L14107, doi:10.1029/2006GL026294.

Liemohn, M. W., J. U. Kozyra, V. K. Jordanova, G. V. Khazanov, M. F. Thomsen, and T. E. Cayton (1999), Analysis of early phase ring current recovery mechanisms during geomagnetic storms, *Geophys. Res. Lett.*, *26*, 2845–2848, doi:10.1029/1999GL900611.

Liemohn, M. W., J. U. Kozyra, M. F. Thomsen, J. L. Roeder, G. Lu, J. E. Borovsky, and T. E. Cayton (2001), Dominant role of the asymmetric ring current in producing the storm time *Dst**, *J. Geophys. Res.*, *106*, 10,883–10,904, doi:10.1029/2000JA000326.

Liemohn, M. W., S. Xu, S. Yan, M.-C. Fok, and Q. Zheng (2012), Time scales for localized radiation belt injections to become a thin shell, in *Dynamics of the Earth's Radiation Belts and Inner Magnetosphere*, *Geophys. Monogr. Ser.*, vol. 199, edited by D. Summers, et al., pp. 161–175, AGU, Washington, D. C., doi:10.1029/2012GM001335.

Lyons, L. R. (1973), Comments on pitch angle diffusion in the radiation belts, *J. Geophys. Res.*, *78*, 6793–6797, doi:10.1029/JA078i028p06793.

Mauk, B. H., et al. (2012), Science objectives and rationale for the Radiation Belt Storm Probes mission, *Space Sci. Rev.*, doi:10.1007/s11214-012-9908-y.

McComas, D. J., N. Buzulukova, M. G. Connors, M. A. Dayeh, J. Goldstein, H. O. Funsten, S. Fuselier, N. A. Schwadron, and P. Valek (2012), Two Wide-Angle Imaging Neutral-Atom Spectrometers and Interstellar Boundary Explorer energetic neutral atom imaging of the 5 April 2010 substorm, *J. Geophys. Res.*, *117*, A03225, doi:10.1029/2011JA017273.

Meng, X., G. Toth, A. Glocer, M.-C. Fok, and T. I. Gombosi (2013), Pressure anisotropy in global magnetospheric simulations: Coupling with ring current models, *J. Geophys. Res. Space Physics*, *118*, 5639–5658, doi:10.1002/jgra.50539.

Meredith, N. P., R. B. Horne, R. M. Thorne, D. Summers, and R. R. Anderson (2004), Substorm dependence of plasmasphere hiss, *J. Geophys. Res.*, *109*, A06209, doi:10.1029/2004JA010387.

Meredith, N. P., R. B. Horne, A. Sicard-Piet, D. Boscher, K. H. Yearby, W. Li, and R. M. Thorne (2012), Global model of lower band and upper band chorus from multiple satellite observations, *J. Geophys. Res.*, *117*, A10225, doi:10.1029/2012JA017978.

Mitchell, D. G., et al. (2013), Radiation Belt Storm Probes Ion Composition Experiment (RBSPICE), *Space Sci. Rev.*, *179*, 263–308, doi:10.1007/s11214-013-9965-x.

Moldwin, M. B., L. Downward, H. K. Rassoul, R. Amin, and R. R. Anderson (2002), A new model of the location of the plasmapause: CRRES results, *J. Geophys. Res.*, *107*(A11), 1339, doi:10.1029/2001JA009211.

Möstl, C., M. Temmer, T. Rollett, C. J. Farrugia, Y. Liu, A. M. Veronig, M. Leitner, A. B. Galvin, and H. K. Biernat (2010), STEREO and Wind observations of a fast ICME flank triggering a prolonged geomagnetic storm on 5–7 April 2010, *Geophys. Res. Lett.*, *37*, L24103, doi:10.1029/2010GL045175.

Nagai, T. (2012), Rebuilding process of the outer electron radiation belt: The spacecraft Akebono observations, in *Dynamics of the Earth's Radiation Belts and Inner Magnetosphere*, *Geophys. Monogr. Ser.*, vol. 199, AGU, Washington, D. C., doi:10.1029/2012GM001281.

O'Brien, T. P., K. R. Lorentzen, I. R. Mann, N. P. Meredith, J. B. Blake, J. F. Fennell, M. D. Looper, D. K. Milling, and R. R. Anderson (2003), Energization of relativistic electrons in the presence of ULF power and MeV microbursts: Evidence for dual ULF and VLF acceleration, *J. Geophys. Res.*, *108*(A8), 1329, doi:10.1029/2002JA009784.

Ohtani, S., Y. Miyoshi, H. J. Singer, and J. M. Weygand (2009), On the loss of relativistic electrons at geosynchronous altitude: Its dependence on magnetic configurations and external conditions, *J. Geophys. Res.*, *114*, A01202, doi:10.1029/2008JA013391.

Rairden, R. L., L. A. Frank, and J. D. Craven (1986), Geocoronal imaging with Dynamics Explorer, *J. Geophys. Res.*, *91*, 13,613–13,630, doi:10.1029/JA091iA12p13613.

Reeves, G. D., K. L. McAdams, and R. H. W. Friedel (2003), Acceleration and loss of relativistic electrons during geomagnetic storms, *Geophys. Res. Lett.*, *30*(10), 1529, doi:10.1029/2002GL016513.

Reeves, G. D., S. K. Morley, R. H. W. Friedel, M. G. Henderson, T. E. Cayton, G. Cunningham, J. B. Blake, R. A. Christensen, and D. Thomsen (2011), On the relationship between relativistic electron flux and solar wind velocity: Paulikas and Blake revisited, *J. Geophys. Res.*, *116*, A02213, doi:10.1029/2010JA015735.

Robinson, R. M., R. R. Vondrak, K. Miller, T. Dabbs, and D. A. Hardy (1987), On calculating ionospheric conductances from the flux and energy of precipitating electrons, *J. Geophys. Res.*, *92*(A3), 2565–2569, doi:10.1029/JA092iA03p02565.

Roelof, E. C. (1997), ENA emission from nearly-mirroring magnetospheric ions interacting with the exosphere, *Adv. Space Res.*, *20*, 361–366.

Roelof, E. C., and D. J. Williams (1988), The terrestrial ring current: From in situ measurements to global images using energetic neutral atoms, *John Hopkins APL Tech. Dig.*, *9*, 144–163.

Saito, S., Y. Miyoshi, and K. Seki (2010), A split in the outer radiation belt by magnetopause shadowing: Test particle simulations, *J. Geophys. Res.*, *115*, A08210, doi:10.1029/2009JA014738.

Sheldon, R. B., and D. C. Hamilton (1993), Ion transport and loss in the Earth's quiet ring current, 1, data and standard model, *J. Geophys. Res.*, *98*, 13,491–13,508, doi:10.1029/92JA02869.

Sibeck, D. G., and V. Angelopoulos (2008), THEMIS science objectives and mission phases, *Space Sci. Rev.*, *141*, 35–59.

Sotirelis, T., and P. T. Newell (2000), Boundary-oriented electron precipitation model, *J. Geophys. Res.*, *105*, 18,655–18,673, doi:10.1029/1999JA000269.

Spence, H. E., et al. (2013), Science goals and overview of the Radiation Belt Storm Probes (RBSP) Energetic Particle, Composition, And Thermal Plasma (ECT) suite on NASA's Van Allen Probes mission, *Space Sci. Rev.*, *179*, 311–336, doi:10.1007/s11214-013-0007-5.

Summers, D., C. Ma, N. P. Meredith, R. B. Horne, R. M. Thorne, D. Heynderickx, and R. R. Anderson (2002), Model of the energization of out-zone electrons by whistler mode chorus during the October 9, 1990 geomagnetic storm, *Geophys. Res. Lett.*, *29*(24, 2174), doi:10.1029/2002GL016039.

Summers, D., B. Ni, and N. P. Meredith (2007), Timescales for radiation belt electron acceleration and loss due to resonant wave particle interactions: 2. Evaluation for VLF chorus, ELF hiss, and EMIC waves, *J. Geophys. Res.*, *112*, A04207, doi:10.1029/2006JA011993.

Takagi, S., T. Nakamura, T. Kohno, N. Shiono, and F. Makino (1993), Observation of space radiation environment with EXOS-D, *IEEE Trans. Nucl. Sci.*, *40*, 1491–1497.

Toffoletto, F. R., S. Sazykin, R. Spiro, and R. Wolf (2003), Inner magnetospheric modeling with the Rice Convection Model, *Space Sci. Rev.*, *107*, 175–196.

Tsyganenko, N. A., and T. Mukai (2003), Tail plasma sheet models derived from Geotail particle data, *J. Geophys. Res.*, *108*(A3), 1136, doi:10.1029/2002JA009707.

Tsyganenko, N. A., and M. I. Sitnov (2005), Modeling the dynamics of the inner magnetosphere during strong geomagnetic storms, *J. Geophys. Res.*, *110*, A03208, doi:10.1029/2004JA010798.

Tsyganenko, N. A., H. J. Singer, and J. C. Kasper (2003), Storm time distortion of the inner magnetosphere: How severe can it get?, *J. Geophys. Res.*, *108*(A5), 1209, doi:10.1029/2002JA009808.

Turner, D. L., Y. Shprits, M. Hartinger, and V. Angelopoulos (2012), Explaining sudden losses of outer radiation belt electrons during geomagnetic storms, *Nat. Phys.*, *8*, 208–212, doi:10.1038/nphys2185.

Turner, N. E., W. D. Cramer, S. K. Earles, and B. A. Emery (2009), Geoefficiency and energy partitioning in CIR-driven and CME-driven storms, *J. Atmos. Sol. Terr. Phys.*, *71*, 1023–1031, doi:10.1016/j.jastp.2009.02.005.

Ukhorskiy, A. Y., B. J. Anderson, P. C. Brandt, and N. A. Tsyganenko (2006), Storm time evolution of the outer radiation belt: Transport and losses, *J. Geophys. Res.*, *111*, A11S03, doi:10.1029/2006JA011690.

Van Allen, J. A. (1959), The geomagnetically trapped corpuscular radiation, *J. Geophys. Res.*, *64*, 1683–1689, doi:10.1029/JZ064i011p01683.

Vette, J. I. (1991), The AE-8 trapped electron model environment, NSSDC/WDC-A-R&S 91–24, NASA Goddard Space Flight Center, Greenbelt, Md., Nov. 1991.

Weimer, D. R. (2001), An improved model of ionospheric electric potentials including substorm perturbations and applications to the Geospace environment modeling November 24, 1996, event, *J. Geophys. Res.*, *106*, 407–416, doi:10.1029/2000JA000604.

Young, S. L., R. E. Denton, B. J. Anderson, and M. K. Hudson (2008), Magnetic field line curvature induced pitch angle diffusion in the inner magnetosphere, *J. Geophys. Res.*, *113*, A03210, doi:10.1029/2006JA012133.

Yu, Y., J. Koller, and S. K. Morley (2013), Quantifying the effect of magnetopause shadowing on electron radiation belt dropouts, *Ann. Geophys.*, *31*, 1929–1939, doi:10.5194/angeo-31-1929-2013.

Zaharia, S. V., V. K. Jordanova, M. F. Thomsen, and G. D. Reeves (2006), Self-consistent modeling of magnetic fields and plasma in the inner magnetosphere: Application to a geomagnetic storm, *J. Geophys. Res.*, *111*, A11S14, doi:10.1029/2006JA011619.

Zheng, Y., M.-C. Fok, and G. V. Khazanov (2003), A radiation belt-ring current forecasting model, *Space Weather*, *1*(3), 1013, doi:10.1029/2003SW000007.